



## OPEN Three-dimensional large eddy simulation of hydrodynamics in multi-pier tandem bridge systems

Wei-qun Liang, Xiaobin Chen✉, Lubo Tang, Jiasheng Zhang & Jun Cheng

The wake flow generated by tandem bridge piers significantly interferes with downstream flow fields, resulting in complex hydrodynamic interactions that impact structural safety and durability. This study employs large eddy simulation (LES) to investigate the three-dimensional hydrodynamic characteristics of eight equally spaced tandem bridge piers under varying flow velocities (0.5–1.5 m/s), spacing ratios (1.5–3.5), and pier numbers (2–10). The results indicate that, under typical conditions, the upstream piers exhibit the highest pressure, which decreases along the flow direction, while the pressure extrema of downstream piers shift laterally. The velocity distribution is asymmetric, and vortex structures evolve from high-intensity small scales to moderate expansion and low-intensity diffusion. The lift coefficient fluctuates periodically with spatial lag, and the drag coefficient shows complex variations, including negative drag on some piers. The downstream vortex shedding frequency decreases, accompanied by multifrequency resonance. Increasing flow velocity stabilizes lift responses for upstream and midstream piers, with the main vortex shedding frequency increasing most in the upstream region and multifrequency phenomena shifting upstream. Larger spacing ratios reduce flow interference, enhance vortex shedding frequencies upstream, and strengthen multifrequency resonance, with triple-frequency resonance observed at terminal piers. An increase in the number of piers improves flow field stability, reduces peak lift, and decreases the occurrence of negative drag. These findings provide theoretical support for bridge monitoring and protection.

**Keywords** Tandem bridge piers, Hydrodynamics, Large eddy simulation, Lift coefficient, Drag coefficient, Vortex shedding frequency

Bridges are vital elements of modern transportation infrastructure, serving indispensable roles in highway and railway networks. With rapid urbanization and growing traffic demands, bridge designs increasingly feature wider decks and more densely arranged piers, making multi-pier tandem structures more common in engineering practice<sup>1,2</sup>. The hydrodynamic behavior of tandem bridge piers is closely linked to structural safety and durability, and directly affects scour protection and maintenance strategies<sup>3–5</sup>.

In recent years, extensive experimental and numerical studies have addressed flow disturbances, local scour, and vortex evolution associated with isolated, tandem, and staggered pier configurations<sup>6–9</sup>. Key hydrodynamic parameters such as lift coefficient (CL), drag coefficient (CD), and vortex shedding frequency are widely used to evaluate pier forces and flow field disruptions<sup>10,11</sup>. Compared to single piers, the wake from upstream piers in tandem arrangements creates complex interference for downstream piers, resulting in distinct hydrodynamic responses<sup>12,13</sup>. For instance, Ataie-Ashtiani and Aslani-Kordkandi<sup>14</sup> experimentally revealed strong upwelling and turbulence variation in tandem pier gaps; Azma et al.<sup>4</sup> used 3D simulations and machine learning to analyze flow structure and bed shear stress evolution under multi-pier conditions. Pasupuleti et al.<sup>3,6</sup> studied recirculation zones, vortex systems, and horseshoe vortex intensity for tandem and staggered piers in both mobile and rigid bed scenarios, providing insights for scour protection. Gao et al.<sup>7</sup> and Wang et al.<sup>8</sup> further explored scour pit development and fluid structure limits around tandem piers under different scouring environments. In summary, existing studies have clarified many local hydrodynamic features of tandem piers, but comprehensive understanding of multi-pier system responses is still limited.

Research on overall hydrodynamics in multi-pier systems is progressing. Sharifi Ghazijahani and Cierpka<sup>9</sup> identified, via PIV experiments, three flow regimes—single bluff body, transitional, and synchronized vortex shedding—in cylinder arrays, with vortex frequency and synchronization varying with spacing, influencing heat transfer and structural loads. Qi et al.<sup>10</sup> highlighted the impact of pier spacing on near-bed velocity and scour risk. Das et al.<sup>15</sup> and Liu et al.<sup>16</sup> proposed predictive formulas for scour depth and critical velocity in

School of Civil Engineering, Central South University, Changsha 410083, China. ✉email: chen\_xiaobin@csu.edu.cn

multi-pier configurations, improving engineering assessments. Advances in simulation methods have also enhanced hydrodynamic analysis: RANS models are efficient near walls, while LES better captures complex vortex structures and large-scale turbulence, making it suitable for multi-pier tandem systems<sup>12,13,17</sup>. Hashemi et al.<sup>17</sup> and Kumari et al.<sup>12,13</sup> validated the accuracy of RNG k- $\epsilon$  and LES models for tandem pier flows and scour prediction, with LES excelling in simulating complex wakes and unsteady vortex shedding. Yu et al.<sup>18</sup> introduced self-sustaining inlet turbulent boundary conditions to improve consistency between simulations and experiments, and developed a simplified prediction method based on shielding coefficients. Overall, technical progress has deepened multi-pier hydrodynamics research, but systematic insights into the evolution, spectral response, and spatial partitioning of complex systems (six or more piers) are still lacking<sup>9</sup>.

Additionally, parameters such as flow velocity, spacing ratio ( $S/D$ ), and pier number ( $n$ ) significantly affect tandem pier hydrodynamics<sup>19,20</sup>. Different combinations can alter force distribution, wake structure, and vortex shedding, and may lead to phenomena like negative drag, multi-frequency resonance, and delayed lift/drag transmission, increasing flow field complexity<sup>21–23</sup>. Nandi and Das<sup>19</sup> proposed predictive equations for maximum scour depth near tandem, side-by-side, and eccentric piers, achieving high accuracy. Mamoon et al.<sup>20</sup> found that arrangement affects scour evolution and maximum depth, aiding protective design. Recent studies on vortex structures and flow partitioning continue to enrich the field. Zhou et al.<sup>21,24</sup> analyzed vortex evolution and Strouhal number changes in side-by-side and near-wall cylinder wakes, revealing gap flow deflection effects. Guo et al.<sup>22</sup> and Sumner et al.<sup>23</sup> identified various flow patterns and spatial differences in vortex shedding frequency in staggered cylinder arrays. Raushan et al.<sup>25</sup> and Golpira et al.<sup>26</sup> examined how bluff body geometry and submergence ratio influence wake turbulence and ecological impacts. While parameter and vortex mechanism studies are advancing, further investigation into spatial distribution and partitioning in multi-pier tandem systems is needed.

Despite considerable progress, systematic understanding of overall hydrodynamic response, vortex shedding frequency distribution, and flow field partitioning for three-dimensional, evenly spaced tandem bridge piers with six or more units remains insufficient. In this study, three-dimensional large eddy simulation (LES) is used to analyze eight evenly spaced tandem bridge piers under varying flow velocities, spacing ratios, and pier numbers. The focus is on the spatial distribution of lift and drag coefficients, vortex shedding frequency, multi-frequency resonance, and flow field partitioning. The results provide theoretical support for bridge health monitoring, fatigue life assessment, and optimization of protective measures.

## Methodology

### Geometric modeling

Figure 1 presents the three-dimensional model and computational domain for the bridge pier array. The model consists of eight circular piers, each with a diameter of 1 m. The piers are aligned in a row along the flow direction, with a center-to-center spacing of 2.5 m. The computational domain measures 36 m in length, 10 m in width, and 3 m in height, which is sufficient for flow development and wake analysis. The inlet flow velocity

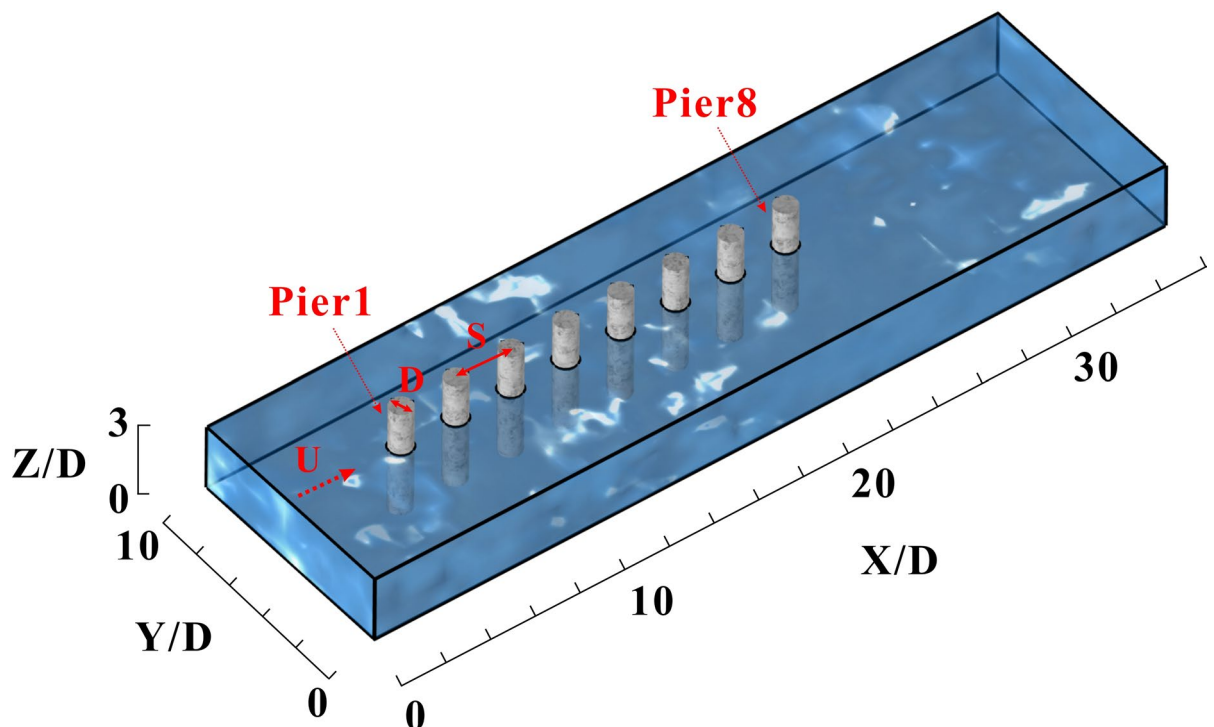


**Fig. 1.** Three-dimensional geometric model and computational domain of the bridge pier array.

is set to match the direction of the pier arrangement, simulating actual river conditions. The piers are numbered sequentially from 1 to 8, starting from upstream to downstream.

### Governing equations

The Large Eddy Simulation (LES) turbulence model is adopted to analyze the hydrodynamic characteristics of the flow field around bridge pier arrays. LES is a numerical method for turbulence that separates large-scale and small-scale turbulent structures in the flow field through spatial filtering. LES can directly resolve the large-scale vortex structures that dominate the flow, while the effects of small-scale turbulence are approximated using the Subgrid-Scale (SGS) model. Compared with the traditional Reynolds-Averaged Navier-Stokes (RANS) model, LES offers higher accuracy and physical fidelity in capturing transient vortex shedding, wake interference, and other complex flow phenomena, making it particularly suitable for numerical studies of highly turbulent regions such as bridge pier arrays.

The governing equations of LES are based on the filtered incompressible Navier–Stokes equations, expressed as follows:

$$\frac{\partial \bar{u}_i}{\partial t} + \frac{\partial (\bar{u}_i \bar{u}_j)}{\partial x_j} = -\frac{1}{\rho} \frac{\partial \bar{p}}{\partial x_i} + \nu \frac{\partial^2 \bar{u}_i}{\partial x_j^2} - \frac{\partial \tau_{ij}}{\partial x_j} \quad (1)$$

where  $\bar{u}_i$  is the filtered velocity component,  $\bar{p}$  is the filtered pressure,  $\rho$  is the fluid density,  $\nu$  is the kinematic viscosity, and  $\tau_{ij}$  is the subgrid-scale stress tensor representing the effects of small-scale turbulence introduced by the filtering process.

The subgrid-scale stress tensor is closed using the Smagorinsky model, given by:

$$\tau_{ij} - \frac{1}{3} \tau_{kk} \delta_{ij} = -2\nu_{sgs} \bar{S}_{ij} \quad (2)$$

where  $\nu_{sgs}$  is the subgrid-scale eddy viscosity, and  $\bar{S}_{ij}$  is the filtered strain rate tensor. In the Smagorinsky model, the subgrid-scale eddy viscosity is defined as:

$$\nu_{sgs} = (C_s \Delta)^2 |\bar{S}| \quad (3)$$

where  $C_s$  is the Smagorinsky constant,  $\Delta$  is the filter width, and  $|\bar{S}|$  is the magnitude of the strain rate tensor.

### Boundary conditions and mesh strategy

Figure 2 illustrates the mesh arrangement and boundary conditions of the computational domain. The left boundary is defined as a velocity inlet, while the right boundary is set as a pressure outlet with a fixed pressure of 0 Pa. The surfaces of the piers and the bottom are treated as no-slip walls. Symmetry boundary conditions are applied to the top and lateral boundaries to ensure physical consistency of the flow field.

Water is used as the working fluid, with a density of 1000 kg/m<sup>3</sup> and a dynamic viscosity of 1.0 × 10<sup>-3</sup> Pa·s. The initial velocity and pressure are set to 0 m/s and 0 Pa, respectively, to realistically represent the physical processes in the tandem pier flow field.

To accurately resolve near-wall turbulence, the distance from the wall to the first mesh node ( $y$ ) is set to 0.02 mm, resulting in a dimensionless wall distance ( $Y^+$ ) of approximately 1. This ensures the first mesh layer is within the viscous sublayer, allowing precise calculation of velocity gradients and turbulent structures near the wall<sup>27</sup>. The calculation of  $Y^+$  is as follows<sup>27</sup>:

$$Y^+ = \frac{u_\tau y}{\nu} \quad (4)$$

where  $u_\tau$  is the friction velocity,  $y$  is the distance from the wall to the first mesh node, and  $\nu$  is the kinematic viscosity.

Mesh sensitivity analysis was conducted for four mesh densities: coarse, medium, fine, and ultra-fine, as summarized in Table 1<sup>28</sup>. The coarse mesh exhibited a relatively high error (3.18%), while the medium and fine meshes yielded errors of 0.95% and 0.24%, respectively, both below 1%. Considering both computational cost and accuracy, the medium mesh was selected for subsequent simulations<sup>27</sup>.

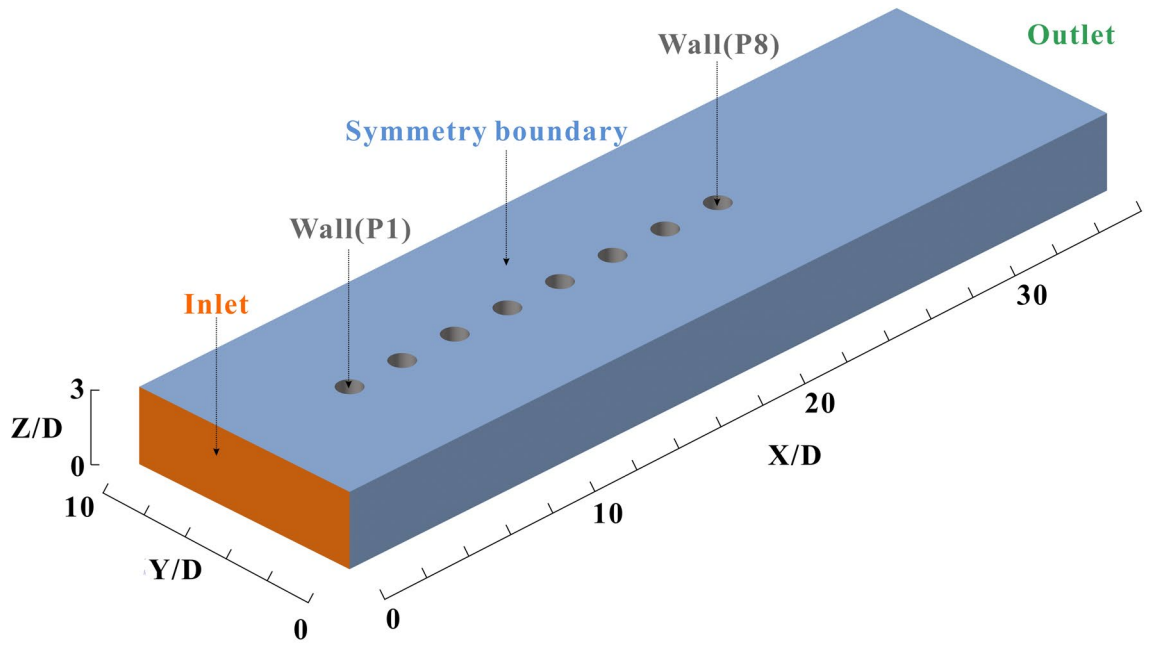
### Hydrodynamic formulas

Hydrodynamic parameters are employed to characterize the flow behavior around the pier, with particular emphasis on the lift coefficient ( $C_L$ ), drag coefficient ( $C_D$ ), and their associated frequency features<sup>29</sup>. The Reynolds number ( $Re$ ) is utilized to describe the flow regime and is defined as follows<sup>30,31</sup>:

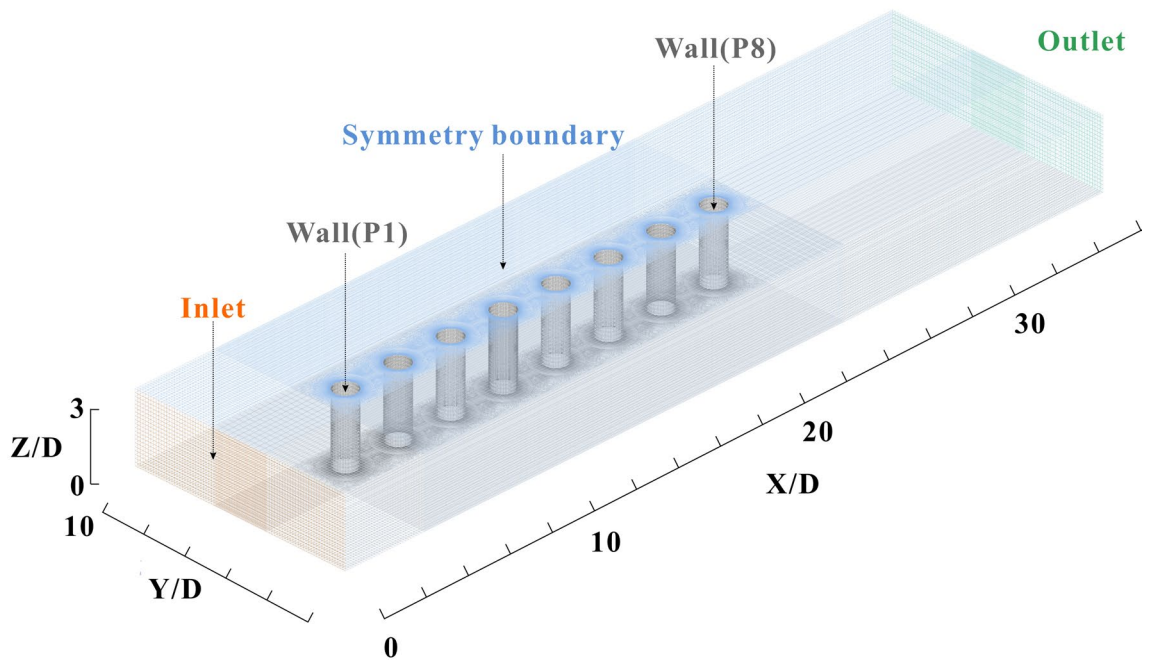
$$Re = \frac{\rho U L}{\mu} \quad (5)$$

where  $\rho$  denotes the fluid density,  $U$  is the characteristic velocity of the flow,  $L$  represents the characteristic length (typically the diameter of the pier), and  $\mu$  is the dynamic viscosity of the fluid.

The lift coefficient ( $C_L$ ) and drag coefficient ( $C_D$ ) are calculated to quantify the hydrodynamic forces acting on the pier<sup>30</sup>. They are given by:



(a)



(b)

**Fig. 2.** Schematic diagram of the boundary conditions and mesh arrangement in the computational domain. (a) Boundary condition setup; (b) Mesh configuration.

Mesh density	Number of elements ( $\times 10^6$ )	Error rate (%)
Coarse mesh	4.06	3.18
Medium mesh	5.11	0.95
Fine mesh	6.03	0.24
Ultra-fine mesh	7.05	N/A

**Table 1.** Results of mesh sensitivity analysis.

$$C_L = \frac{F_L}{\frac{1}{2}\rho U^2 A} \quad (6)$$

$$C_D = \frac{F_D}{\frac{1}{2}\rho U^2 A} \quad (7)$$

where  $F_L$  and  $F_D$  are the lift and drag forces exerted by the fluid on the pier, respectively, and  $A$  is the reference area, typically taken as the projected frontal area of the pier.

To investigate the frequency characteristics of the lift coefficient, a Fast Fourier Transform (FFT) is performed on the time series data of  $C_L$ . The dominant frequency, denoted as  $f_1$ , corresponds to the primary vortex shedding frequency<sup>27</sup>. The amplitudes of the frequency components are denoted as  $A_i$ , where  $A_1$  is the amplitude at the dominant frequency  $f_1$ , and  $A_i$  ( $i = 2, 3, \dots$ ) represent the amplitudes of the secondary frequencies<sup>27,32</sup>. Multi-frequency resonance is identified according to the following criterion:

$$A_i \geq 0.8A_1 \quad (i = 2, 3, \dots) \quad (8)$$

If the amplitude of any secondary frequency component satisfies this condition, multi-frequency resonance is considered to occur. This quantitative criterion enables the identification of complex resonance phenomena in the flow field surrounding the pier.

### Numerical method verification

To validate the accuracy of the present computational method, simulations are conducted to determine the Strouhal number (St) for flow past a circular cylinder at various Reynolds numbers (Re). The simulation results were compared with benchmark data from several studies in the literature, including Ma & Karniadakis (2002), Norberg (2001), Parnaudeau et al. (2008), and Jiang & Cheng (2017)<sup>31,33–35</sup>. As shown in Fig. 3, the computed St values exhibit excellent agreement with the reference data across the entire range of Re considered, with all deviations remaining within  $\pm 10\%$ . This consistent accuracy demonstrates the reliability and robustness of the present simulation approach for predicting vortex shedding characteristics in cylinder wakes.

## Results and discussions

### Analysis of typical eight-pier condition

In the typical case, the inflow velocity ( $U$ ) is 1 m/s, the pier diameter is 1 m, and the kinematic viscosity of water is  $1.0 \times 10^{-6}$  m<sup>2</sup>/s, resulting in a Reynolds number  $Re = 1 \times 10^6$ . The spacing ratio is  $S/D = 2.5$ , with eight piers ( $n = 8$ ) and a simulation time of 50 s. Pressure contours, velocity contours, vorticity contours, lift coefficients (CL), drag coefficients (CD), and vortex shedding frequencies are obtained.

#### Pressure distribution

Figure 4 depicts the pressure distribution of eight tandem bridge piers at 50 s, with panel (a) representing the XY plane and panel (b) the XZ vertical section. Maximum pressure points are primarily located on the upstream face, and the leading pier (P1) exhibits the highest pressure at the centerline due to direct inflow impact. For downstream piers (P2–P8), these maximum pressure points progressively shift from the centerline toward the sides of the piers in a staggered pattern<sup>36</sup>: P2, P4, P6, and P8 toward the positive Y direction, and P3, P5, and P7 toward the negative Y direction. The wake generated by upstream piers significantly affects the flow field around downstream piers, resulting in lateral displacement of maximum pressure points and increased lift forces. Minimum pressure points generally occur opposite the maximum pressure points, displaying a symmetric distribution; however, for P2, influenced by the wake of P1, low-pressure regions also appear near the maximum pressure point. As a result of wake effects, the pressure distribution for downstream piers becomes increasingly complex, with the maximum pressure values decreasing sequentially along the flow direction:  $P1 > P2 > P3 > P4 > P5 > P6 > P7 > P8$ .

In the XZ section, the upstream face of P1 is characterized by a high-pressure region, while the downstream face exhibits a low-pressure region. For downstream piers (P2–P8), the distribution of high and low-pressure regions becomes increasingly complex due to wake effects. For example, P2 presents a low-pressure region on the upstream face and a high-pressure region on the downstream face, while between P4 and P5, high and low-pressure regions alternate, especially in the upper part of the section, and are less pronounced near the bottom, likely due to wall effects. Wake interference among tandem bridge piers markedly alters the pressure distribution characteristics, particularly the location and magnitude of the maximum pressure points.

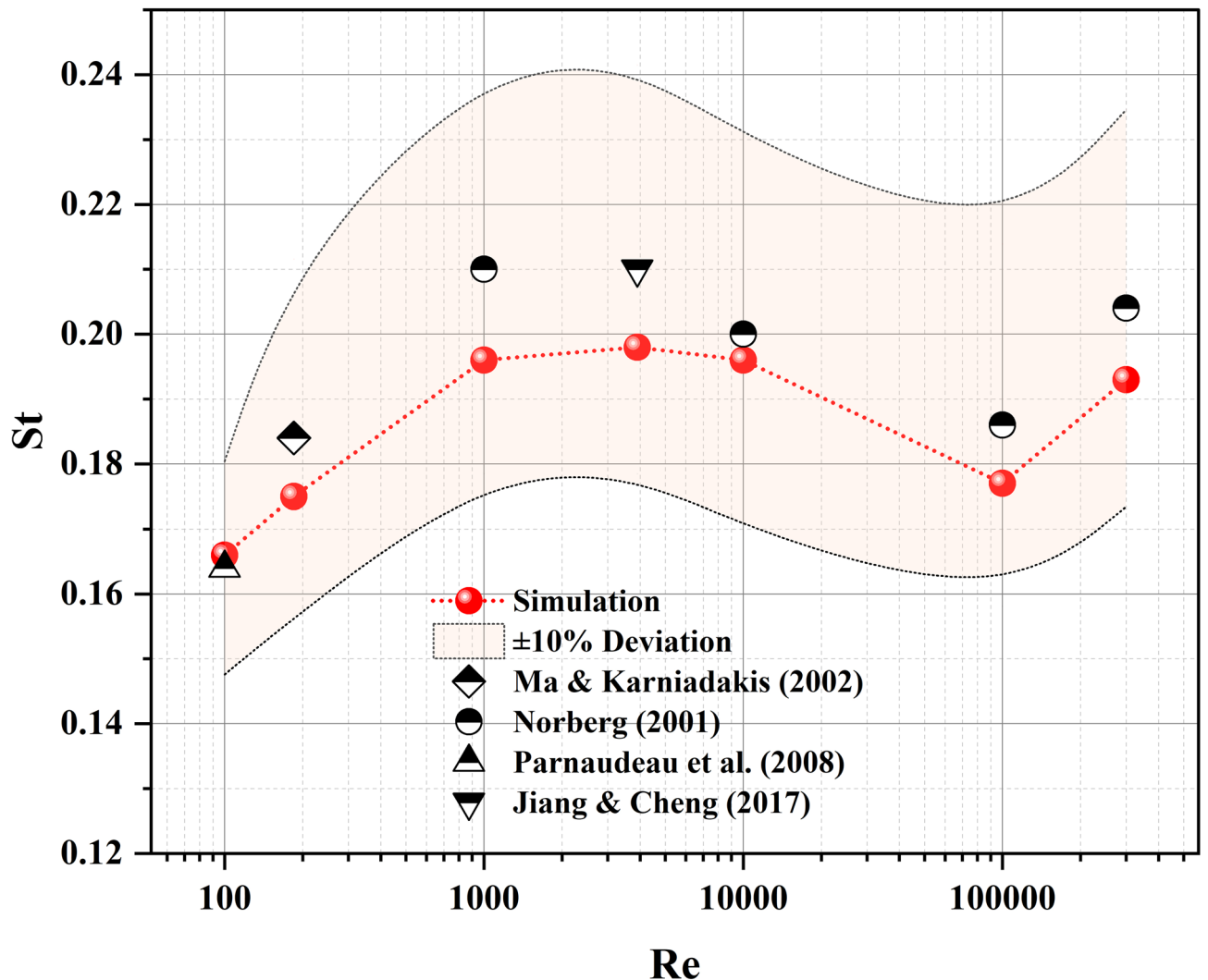


**Fig. 3.** Comparison of Strouhal number ( $St$ ) versus Reynolds number ( $Re$ ) between present simulation results and literature data (Ma & Karniadakis, 2002; Norberg, 2001; Parnaudeau et al., 2008; Jiang & Cheng, 2017).

In summary, wake effects cause both the maximum and minimum pressure points to shift toward the sides of the bridge piers, rather than remaining at the centerline. Furthermore, the magnitude of pressure on tandem bridge piers decreases stepwise from upstream to downstream<sup>36</sup>.

#### Velocity distribution

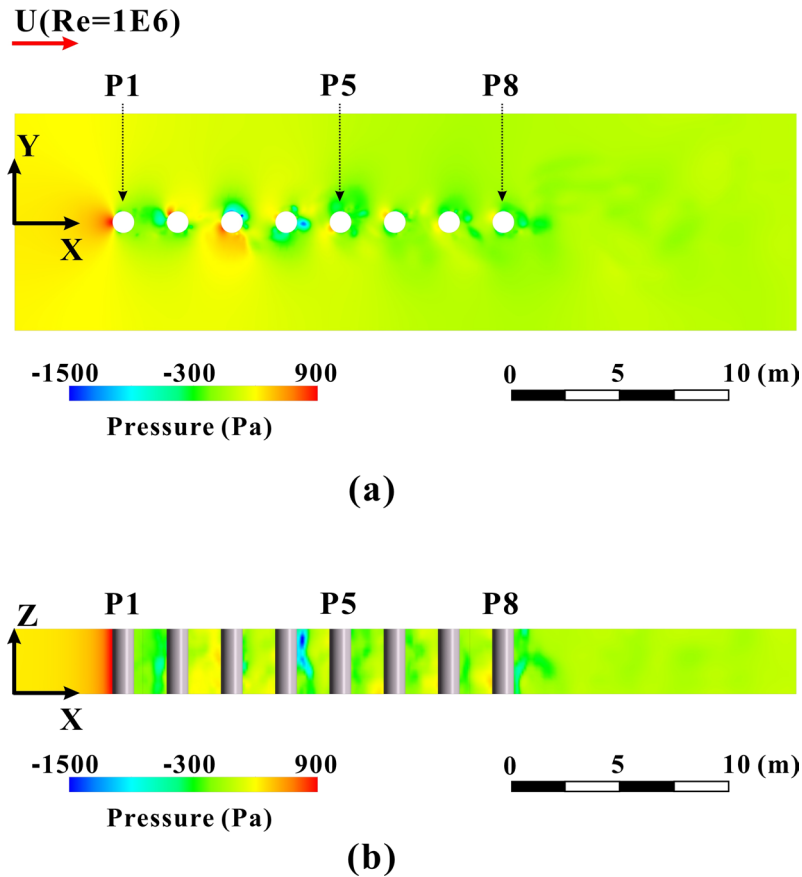
Figure 5 shows the velocity distribution of eight tandem bridge piers at 50 s, including the XY plane (Fig. 5a) and the XZ section (Fig. 5b). In the XY plane, the upstream pier (P1) has reduced velocity on the windward side and increased velocity on both sides of the centerline. The high-velocity zones are symmetrically distributed. A low-velocity recirculation zone forms in the wake of P1, marking the start of vortex shedding<sup>14</sup>. For downstream piers (P2–P8), the velocity distribution is asymmetric. One side has a high-velocity zone, while the other side has a low-velocity zone. These zones alternate on both sides, and the wake shifts toward the sides of the piers<sup>4,28</sup>. For example, the low-velocity wake of P3 deflects toward the negative Y direction. The extent of the low-velocity wake zones decreases in the order: P1 > P8 > P7 > P6 > P5 > P4 > P3 > P2.

Figure 5b presents the velocity distribution in the XZ section. A thin low-velocity layer appears on the windward face of P1. For the following piers, alternating high- and low-velocity regions are observed in the upper and middle areas, with significant variation<sup>10</sup>. Near the riverbed, a thin low-velocity layer forms due to the no-slip boundary.

Overall, tandem piers create complex flow patterns. The velocity distribution on both sides of each pier is asymmetric, with alternating high- and low-velocity zones and deflected wake regions<sup>28,37,38</sup>.

#### Vorticity distribution

Figure 6 presents the vortex clouds of eight tandem bridge piers identified using the Lambda2 criterion. In the XY plane, the vortex structures exhibit a distinct spatial distribution along the series of piers: vortices behind



**Fig. 4.** Pressure distribution of eight tandem bridge piers at 50 s: (a) XY plane; (b) XZ vertical section.

the upstream pier (P1) are smaller in scale but higher in intensity, while those behind the middle piers gradually increase in size with moderate intensity. Downstream piers display the largest and most dispersed vortices, particularly behind P8, where vortex diffusion is most pronounced and intensity further decreases, reflecting the process of vortex diffusion and energy dissipation<sup>37,39</sup>. Additionally, a significant thin layer of strong vortices is observed on the upstream face of P1, covering about 50% of the area, with notable vortices also present on the downstream side. In contrast, the thin layer of strong vortices on the upstream faces of subsequent piers (P2 to P8) is substantially reduced to around 20%, and these layers are distributed in a staggered pattern: P2, P4, P6, and P8 tend toward the positive Y direction, while P3, P5, and P7 shift toward the negative Y direction.

In the XZ vertical section, the vortex distribution does not show obvious stratification, with little difference between the upper and lower regions. Only a thin layer near the riverbed exhibits weaker vorticity, indicating that wall effects suppress vortex generation and development to some extent<sup>39,40</sup>.

Collectively, the vortex cloud maps reveal the evolution of vortex structures among tandem bridge piers, showing clear spatial characteristics: high-intensity, small-scale vortices upstream; moderate-intensity, expanding vortices in the middle; and low-intensity, diffused vortices downstream<sup>28,39,40</sup>. The variation and staggered distribution of thin layers of strong vortices on the upstream faces further highlight the complex influence of tandem piers on the flow field structure.

#### Lift coefficient

Figure 7 shows the time evolution of lift coefficients (CL) for eight tandem bridge piers over a 0–50 s interval. The results indicate that the CL of each pier fluctuates periodically around zero, reflecting the hydrodynamic response to vortex shedding<sup>41</sup>. Spatial analysis reveals that the maximum CL values follow the order: P3 > P2 > P8 > P6 > P4 > P5 > P1 > P7. The peak values for P2, P3, and P8 exceed 1.5. This pattern is mainly attributed to stronger upstream wake effects and vortex interactions acting on the piers located downstream of P1. There is also a clear temporal lag in the occurrence of CL peaks among the piers. This lag indicates that vortex shedding and flow disturbances propagate with a delay along the pier array. Overall, the lift coefficients of tandem piers exhibit periodicity, spatial variation, and temporal lag, emphasizing the complex hydrodynamic interactions induced by vortex shedding in multi-pier configurations<sup>42,43</sup>.

#### Drag coefficient

Figure 8 presents the temporal evolution of drag coefficients (CD) for eight tandem bridge piers (P1–P8) over a 0–50 s interval. All piers exhibit substantial fluctuations in CD, highlighting the dynamic response to flow

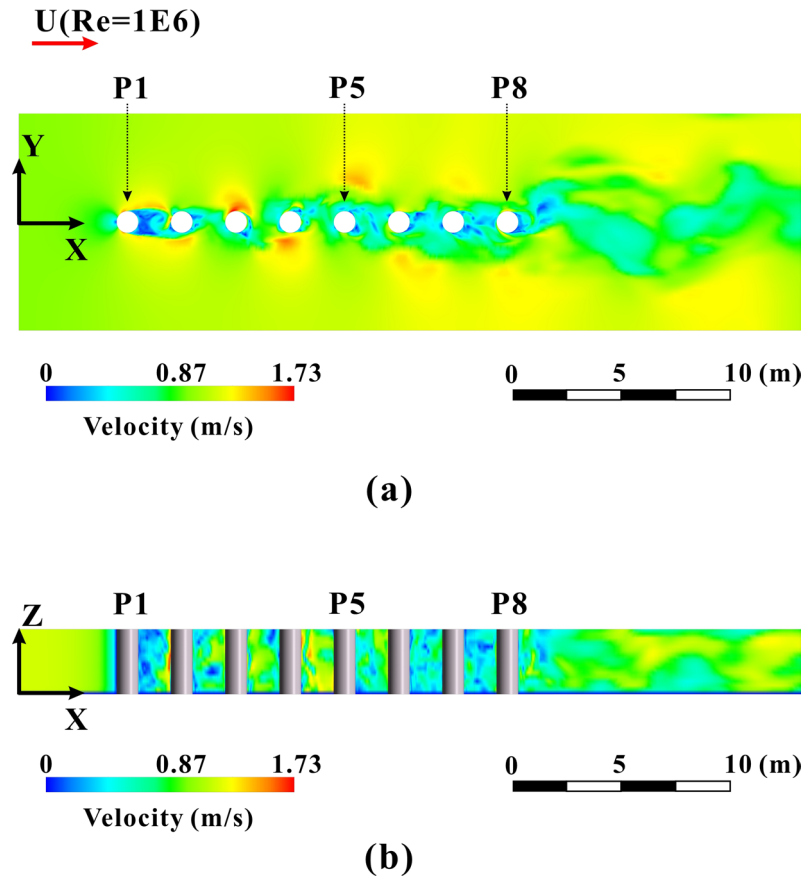


**Fig. 5.** Velocity distribution of eight tandem bridge piers at 50 s: **(a)** XY plane; **(b)** XZ vertical section.

conditions. The average CD values are ranked as follows:  $P1 > P8 > P3 > P7 > P4 > P6 > P2 > P5$ . The leading pier (P1) records the highest mean drag coefficient due to direct exposure to the approaching flow<sup>38</sup>. Importantly, the average CD of downstream piers does not decrease monotonically; several downstream piers (notably P8, P3, and P7) show elevated mean values, suggesting that wake interactions and vortex shedding intensify local drag in the tandem arrangement. The lack of a clear decreasing trend in average CD further underscores the complexity and non-uniformity of flow disturbances induced by the multi-pier configuration<sup>44</sup>.

Negative CD values are observed intermittently, most prominently at P2 and P3, with P7 and P8 also displaying this phenomenon to a lesser extent. These occurrences indicate that, at certain moments, the flow exerts a thrust rather than a drag force on the pier, primarily due to vortex structures and localized reverse flow in the wake region.

#### *Vortex shedding frequency*

Figure 9 presents the vortex shedding frequency distribution of eight piers under typical conditions. The dominant frequency remains stable for piers P1 to P4. The dominant frequency decreases significantly for piers P5 to P8. Upstream piers show higher frequencies, while downstream piers show lower frequencies<sup>14,45</sup>. Multi-frequency resonance occurs at piers P6 and P8. These piers exhibit a secondary frequency  $f_2$  in addition to the dominant frequency  $f_1$ , and the amplitude of  $f_2$  exceeds 80% of  $f_1$ . Under multi-frequency resonance, the dominant frequency  $f_1$  further decreases. For example, the  $f_1$  values at P6 and P8 are lower than those at P5 and P7. This is because the downstream piers are affected by the wake flow from the upstream piers, resulting in reduced vortex shedding frequency and the occurrence of multi-frequency resonance<sup>14,45</sup>.

#### **Effects of inlet velocity**

This section examines eight tandem bridge piers with a spacing ratio of  $S/D = 2.5$ . The inflow velocity ranges from 0.5 to 1.5 m/s, and the Reynolds number varies from  $5 \times 10^5$  to  $1.5 \times 10^6$ . The lift coefficient, drag coefficient, and vortex shedding frequency are analyzed to illustrate the effects of flow velocity on hydrodynamic performance and vortex shedding characteristics of the bridge piers.

#### *Lift coefficient*

Figure 10 shows the distribution of lift coefficients (CL) for eight tandem bridge piers at different flow velocities (Reynolds numbers). The box plots present the mean CL, as well as the maximum and minimum values. As the flow velocity increases, the mean CL of each pier fluctuates around zero. The upstream piers have more stable

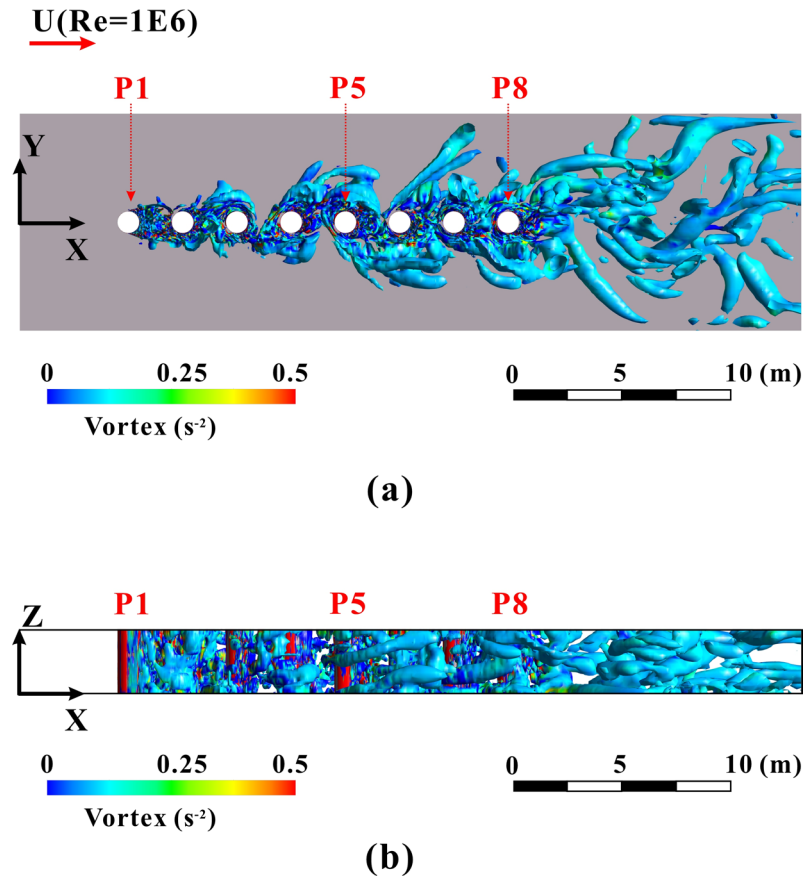


**Fig. 6.** Vortex distribution of eight tandem bridge piers at 50 s: (a) XY plane; (b) XZ vertical section.

mean CL values. The midstream and downstream piers show larger fluctuations, especially at low velocities. When the flow velocity rises, the CL fluctuations of midstream and downstream piers decrease. The lift response becomes more stable. This indicates that the upstream flow field is more stable, while the midstream and downstream regions are more affected by disturbances.

The peak CL values also change with flow velocity. P2, P3, and P4 have higher peaks, indicating stronger vortex-induced lift. P5 to P8 have moderate peaks. P1 has the lowest peak, showing the weakest lift response.

In summary, the lift coefficients of tandem bridge piers at different flow velocities follow a distinct pattern: the upstream flow remains stable, disturbances intensify in the midstream region, and the downstream region gradually returns to stability<sup>12,46</sup>.

#### Drag coefficient

Figure 11 presents box plots of the drag coefficient (CD) for tandem bridge piers under various flow velocities. For P1 and P2, the average CD decreases initially, increases at intermediate velocities, and decreases again at higher velocities. The maximum average CD occurs at 0.5 m/s, while the minimum appears at 0.75 m/s for P2 and at 1.5 m/s for P1. In contrast, P3 to P8 exhibit an opposite trend: the average CD increases to a peak at 0.75 m/s and then decreases, reaching minima at either 0.5–1.5 m/s.

The maximum CD values for each pier fluctuate with flow velocity, showing no clear monotonic pattern. Notably, in some cases, the lower whiskers of the box plots fall below the CD = 0 line, indicating periods when the flow exerts a forward thrust rather than resistance<sup>14,44</sup>. For example, P2 consistently exhibits CD < 0 across all velocities. P3 shows this phenomenon at both low (0.5 m/s) and high (> 1.0 m/s) velocities. P4 and P5 present CD < 0 at 0.75 and 1.25 m/s, P6 at 0.5 and 0.75 m/s, P7 above 1.25 m/s, and P8 at 0.5 m/s. These observations highlight the complexity and variability of hydrodynamic forces in multi-pier configurations.

#### Vortex shedding frequency

Figure 12 presents the variation of vortex shedding frequency for tandem bridge piers under different flow velocities. With increasing flow velocity, the primary frequency (f1) of the lift coefficient for all piers increases. The rate of increase is highest for upstream piers (P1, P2), followed by midstream piers (P4, P5, P6), and lowest for downstream piers (P7, P8)<sup>45</sup>. Some downstream piers, such as P7, exhibit a plateau or fluctuation in frequency rather than a continuous increase.

Multiple frequencies are observed at certain flow velocities for some piers. For instance, downstream piers (P6, P8) show dual-frequency responses at lower velocities (U = 0.5, 1.0 m/s). As the flow velocity rises, the

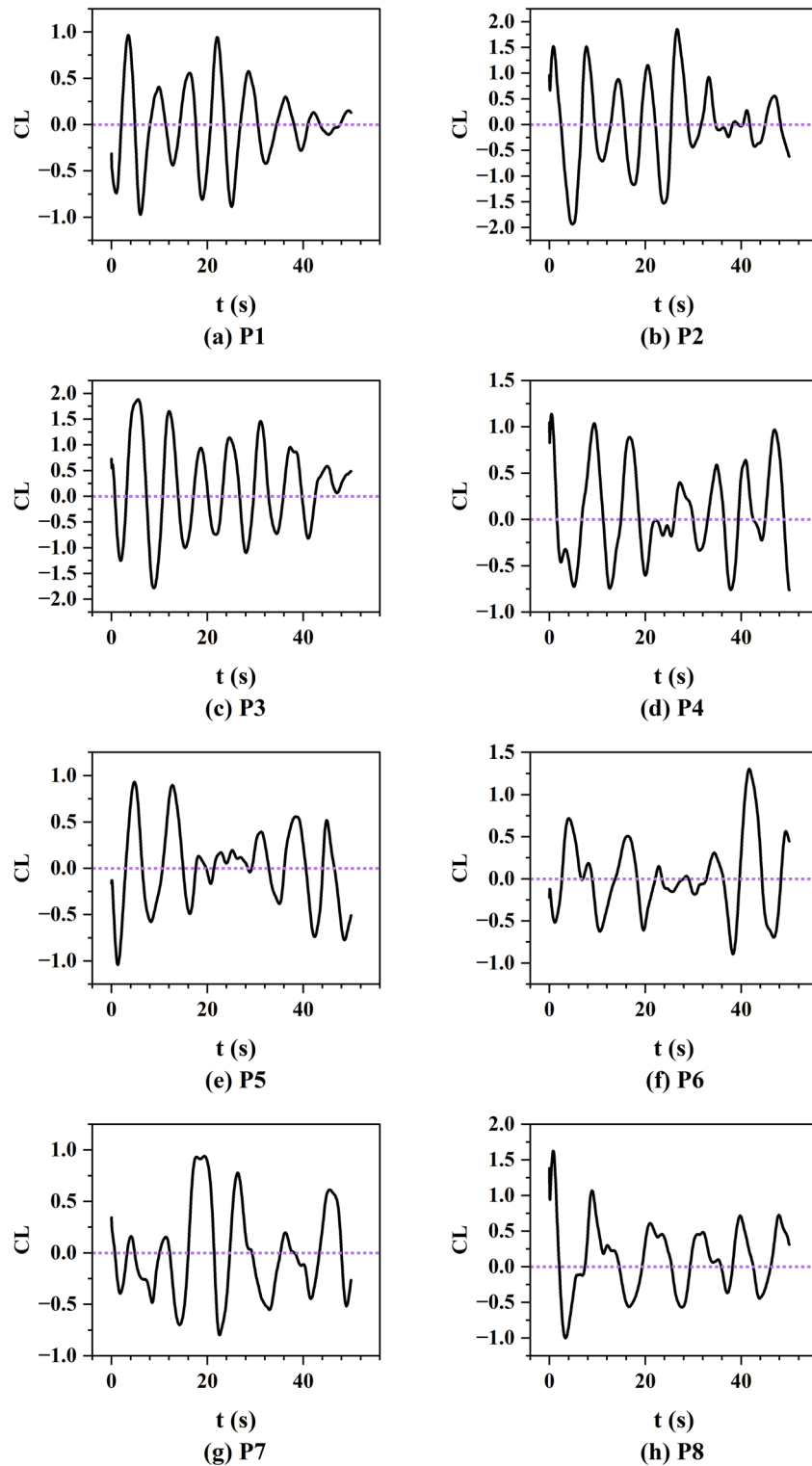


**Fig. 7.** Time histories of lift coefficient (CL) for eight tandem bridge piers from (a) P1 to (h) P8.

occurrence of multiple frequencies shifts to upstream piers (e.g., P1 at  $U = 1.25$  m/s) and then to midstream piers (e.g., P3, P4 at  $U = 1.5$  m/s).

In summary, the primary vortex shedding frequency of the piers increases with flow velocity and Reynolds number. The magnitude of increase is greatest for upstream piers, moderate for midstream piers, and smallest for downstream piers. The location of multi-frequency phenomena shifts from downstream to upstream and then to midstream as the flow velocity increases<sup>45</sup>.

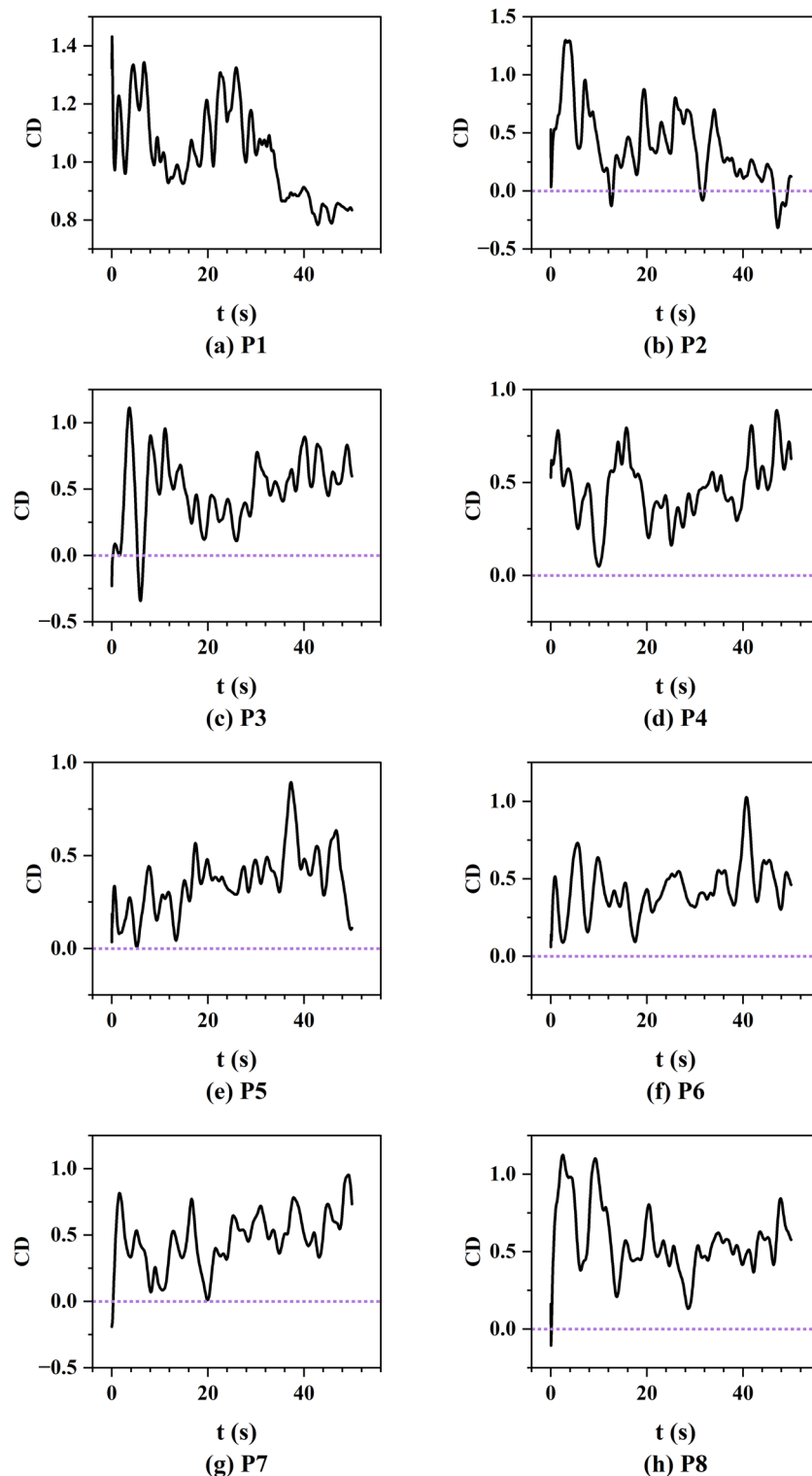


**Fig. 8.** Time histories of the drag coefficient (CD) for eight tandem bridge piers: (a) P1 to (h) P8.

### Effects of spacing ratio

This section examines eight tandem bridge piers under an inflow velocity of 1 m/s, corresponding to a Reynolds number of  $1.0 \times 10^6$ . The spacing ratio ( $S/D$ ) ranges from 1.5 to 3.5. The lift coefficient, drag coefficient, and vortex shedding frequency are analyzed to illustrate the effects of spacing ratio on the hydrodynamic performance and vortex shedding characteristics of the bridge piers.

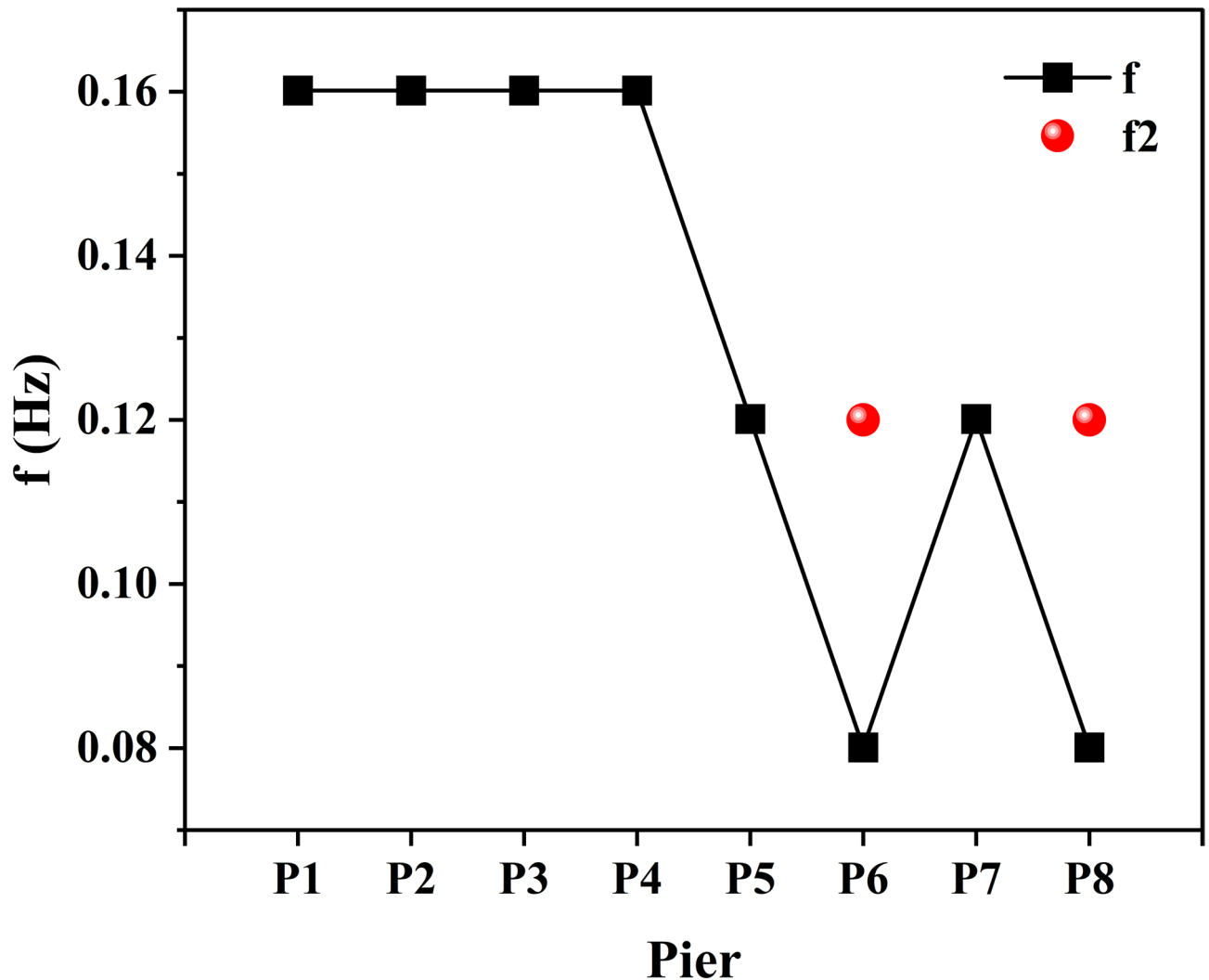


**Fig. 9.** Vortex shedding frequency distribution for eight bridge piers.

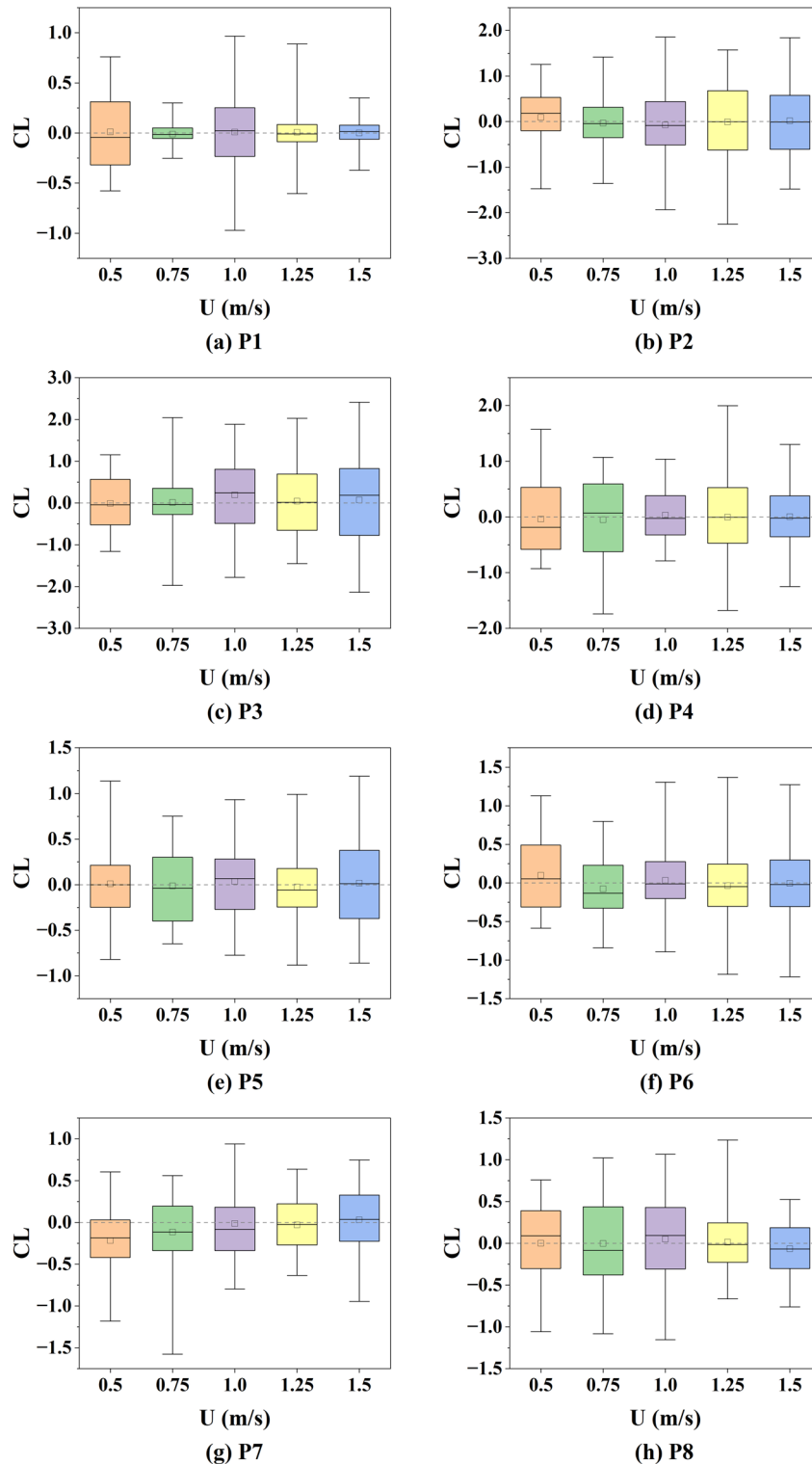
#### Lift coefficient

Figure 13 presents the lift coefficient (CL) for eight tandem bridge piers at various spacing ratios (S/D). The mean CL of the upstream piers (P1 and P2) remains near zero, with little variation as S/D changes. This indicates stable flow conditions around these piers. In contrast, the midstream and downstream piers (P3–P8) exhibit more pronounced fluctuations in mean CL values<sup>47</sup>. Specifically, P3 attains its largest deviation at S/D = 2.5, P4 at S/D = 3.0, and P5 at S/D = 1.5. P6 and P7 exhibit only minor deviations, while P8 shows substantial deviations at S/D = 1.5 and 3.0. Generally, the midstream piers, such as P3, experience the greatest deviations from zero. The downstream piers, like P8, have moderate deviations, and the upstream piers show the least deviation. This pattern indicates that wake effects generated by upstream piers exert a significant influence on the midstream piers.

Additionally, as S/D increases, the peak CL value for P3 initially rises and then falls. The peak CL values for the other piers vary in a nonlinear manner, alternating between increases and decreases as S/D changes. These findings demonstrate that hydrodynamic interactions among the piers are complex, and each pier responds differently to changes in spacing ratio<sup>47</sup>.

#### Drag coefficient

Figure 14 illustrates the variation in drag coefficient (CD) for eight tandem bridge piers under different spacing ratios (S/D). The mean CD for the first pier (P1) remains positive and fluctuates with increasing S/D, reaching a maximum at S/D = 2.5. The mean CD for P2 shows a steady increase as the spacing ratio increases. For P3, the mean CD stabilizes after an initial rise. For P4, the mean CD decreases gradually with increasing S/D and then stabilizes. The mean CD for P5 exhibits a non-monotonic trend, increasing, then decreasing, and rising again. P6 and P7 display a continuous increase in mean CD with larger spacing ratios. The mean CD for P8 initially increases, then decreases, and subsequently rises again.



**Fig. 10.** Distribution of lift coefficients (CL) for eight tandem bridge piers at different flow velocities: (a) P1 to (h) P8.

For peak CD values, P1 and P2 generally increase as S/D increases. P3 reaches a peak and then declines. P4 to P7 show an initial decrease followed by an increase, while P8 demonstrates a pattern of increase, decrease, and subsequent increase.

Negative CD values are observed for some piers under smaller spacing ratios, indicating that local flow conditions generate thrust rather than resistance on the pier surfaces<sup>44,48</sup>. Specifically, negative CD values occur for P2 at S/D ≤ 3, for P3 at S/D = 2.5, for P4 at S/D = 1.5, for P5 at S/D = 1.5, 2, and 3.5, for P6 at S/D = 1.5 and

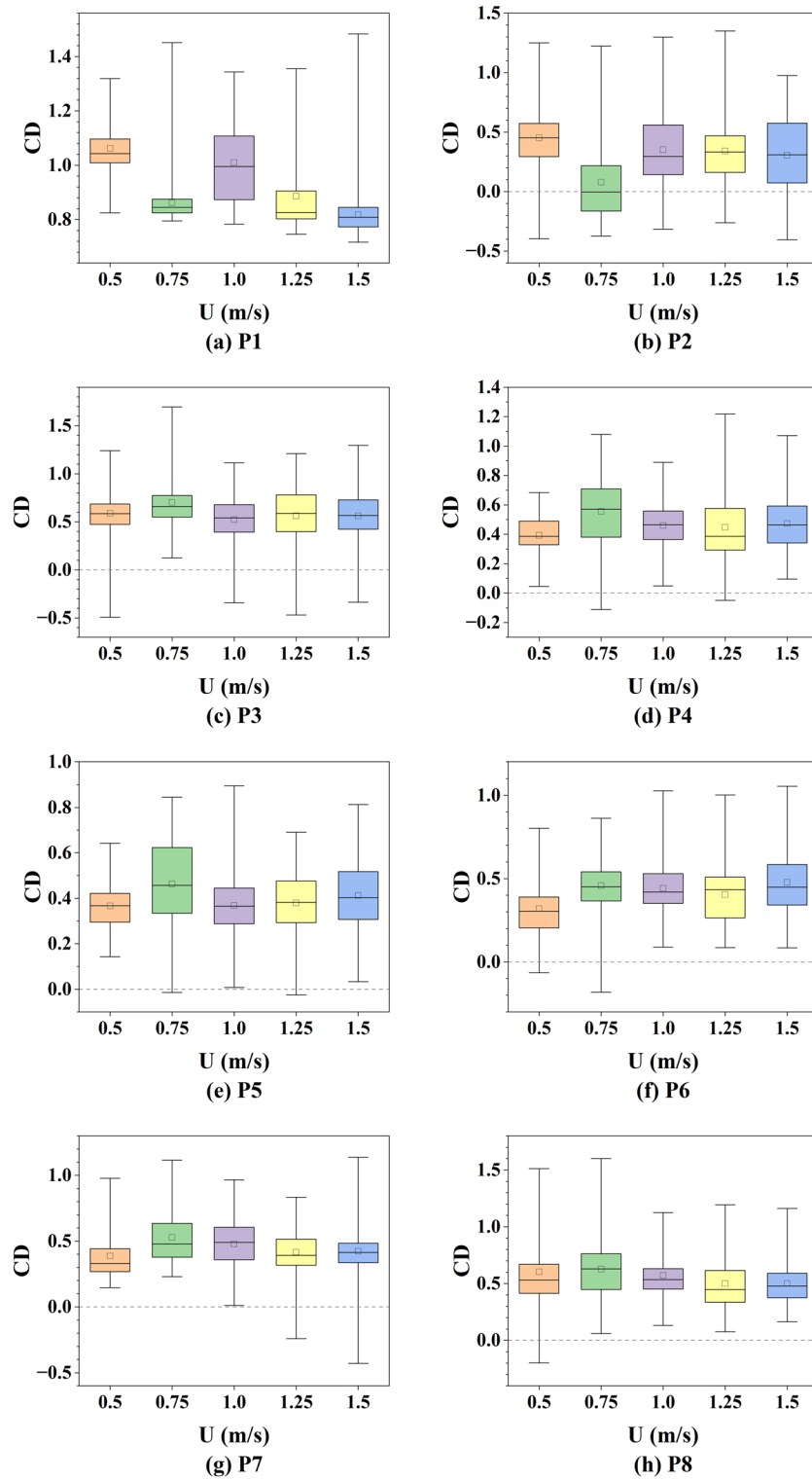


**Fig. 11.** Distribution of drag coefficient (CD) for eight tandem bridge piers under different flow velocities: (a) P1 to (h) P8.

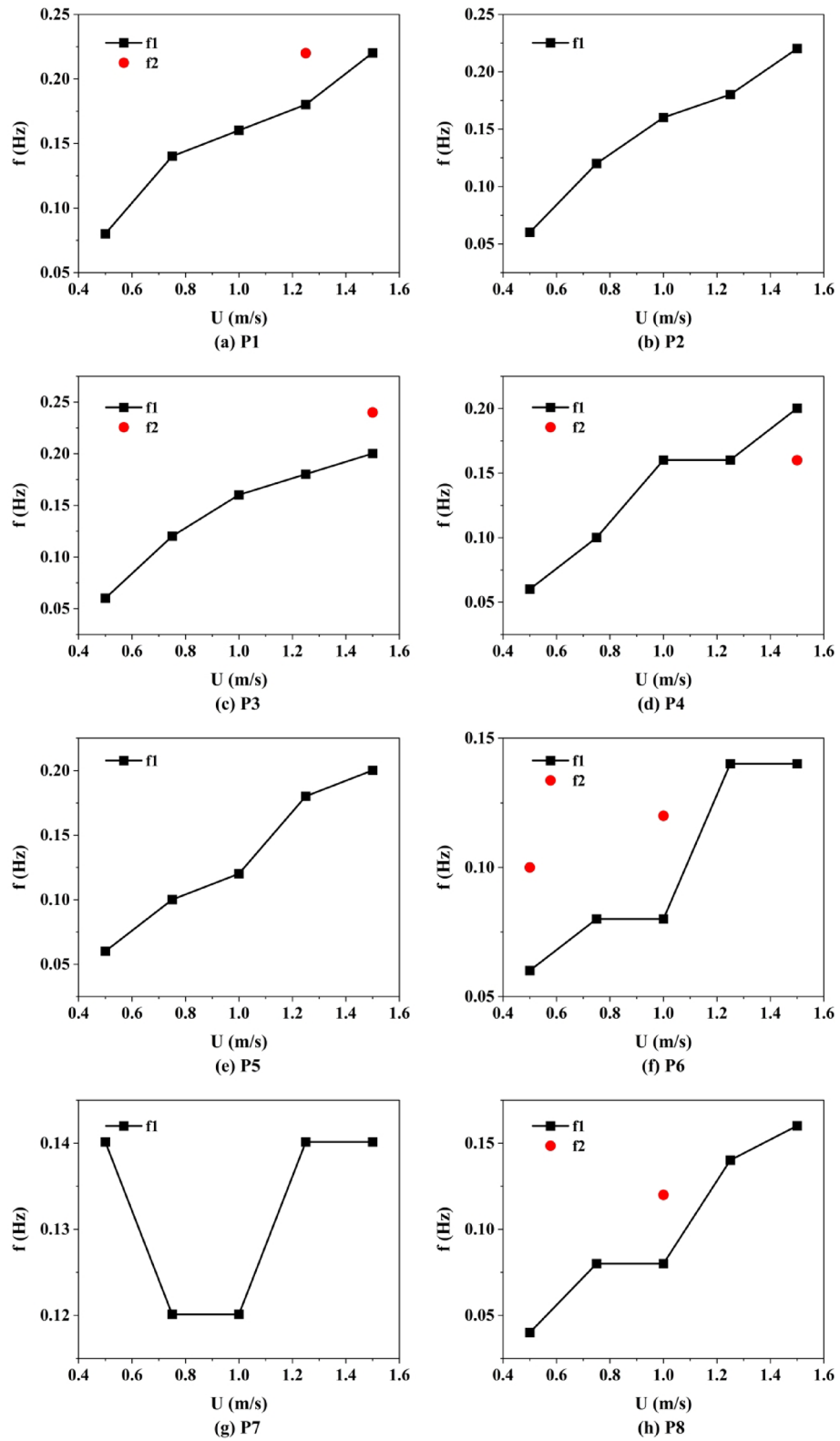


**Fig. 12.** Distribution of vortex shedding frequency for eight tandem bridge piers under different flow velocities: (a) P1 to (h) P8.

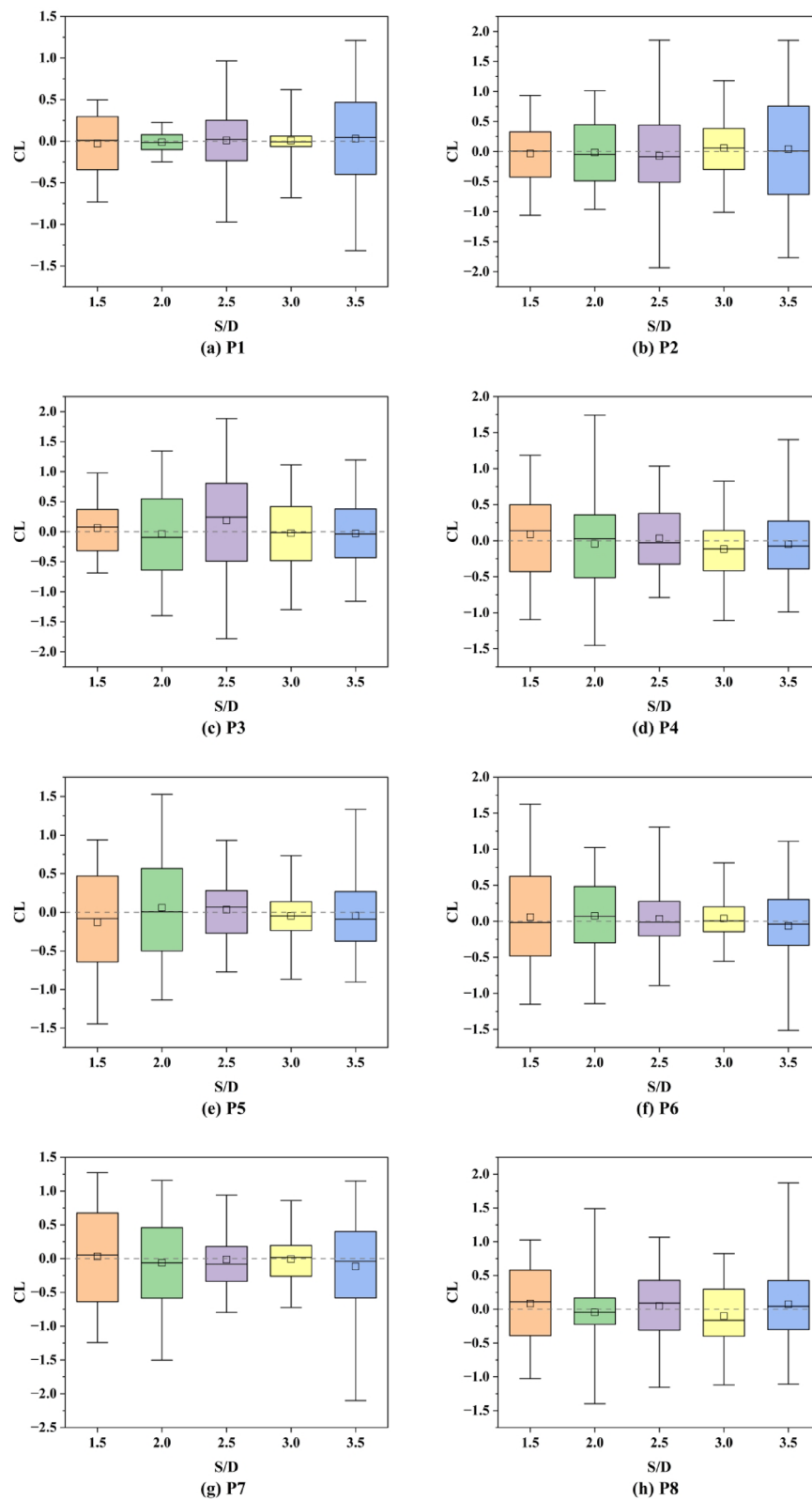


**Fig. 13.** Distribution of lift coefficient (CL) for eight tandem bridge piers under varying spacing ratios (S/D): (a) P1 to (h) P8.

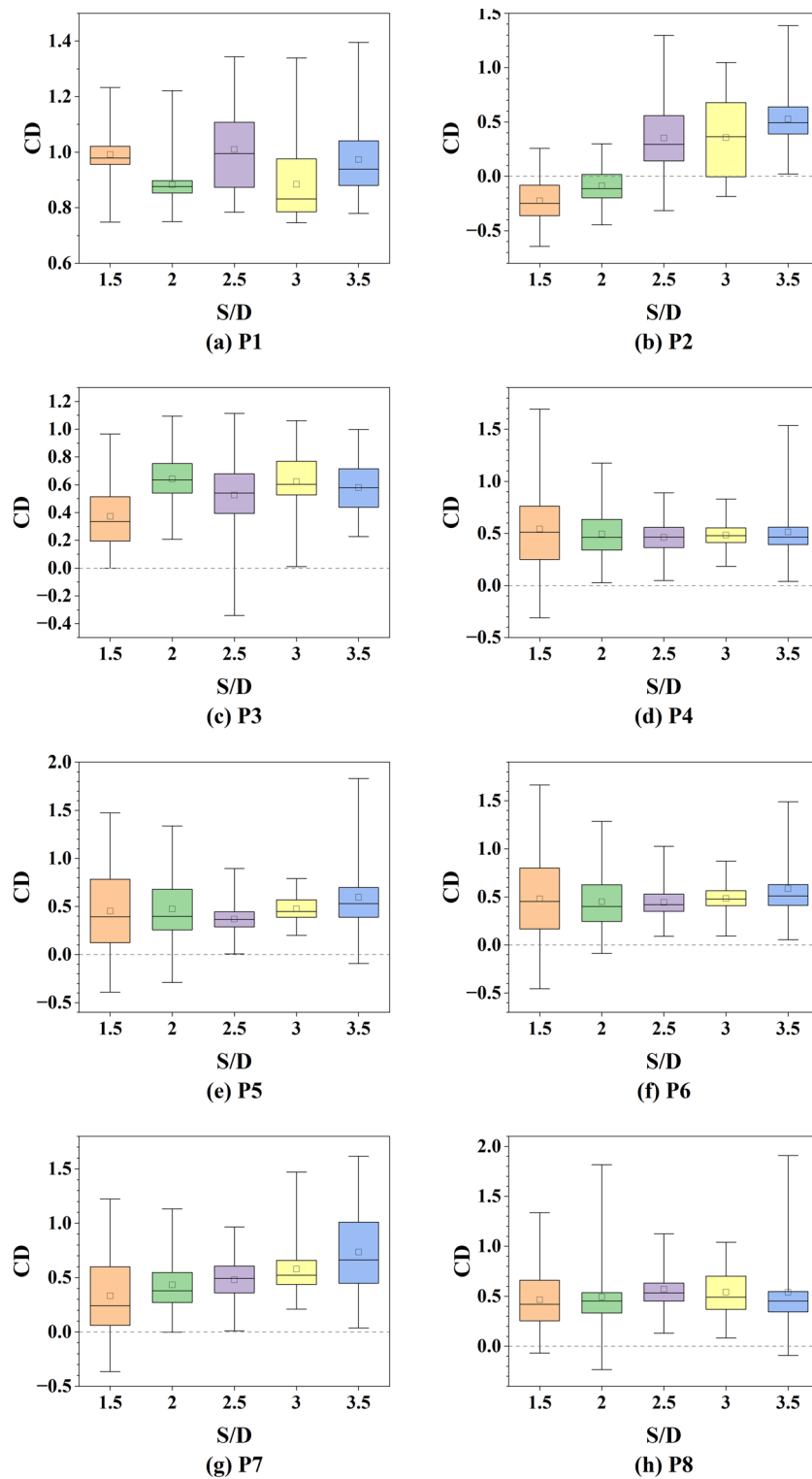


**Fig. 14.** Distribution of drag coefficient (CD) for eight tandem bridge piers under varying spacing ratios (S/D): (a) P1 to (h) P8.

2, for P7 at  $S/D = 1.5$ , and for P8 at  $S/D = 1.5, 2$ , and  $3.5$ . These occurrences are more frequent at smaller spacing ratios and become less common as  $S/D$  increases, suggesting that larger pier spacing effectively reduces flow interference and improves the hydrodynamic performance of the bridge piers.

#### *Vortex shedding frequency*

Figure 15 presents the effects of varying spacing ratios ( $S/D$ ) on the primary frequency of the lift coefficient ( $f_1$ ) and multi-frequency resonance phenomena for eight tandem bridge piers. As  $S/D$  increases, the dominant frequency  $f_1$  generally exhibits an upward trend; however, the magnitude and pattern of change differ among individual piers. Specifically, the upstream piers consistently show the most pronounced frequency enhancement, while the midstream piers demonstrate a non-monotonic pattern, reaching a maximum at  $S/D = 3$ . In contrast, the downstream piers display minor fluctuations without a distinct trend.

Multi-frequency resonance phenomena become increasingly evident with larger  $S/D$  values, particularly in the midstream and downstream piers<sup>49</sup>. The earliest occurrence of multi-frequency resonance is observed at P8 ( $S/D = 2$ ), followed by P6 and P8 ( $S/D = 2.5$ ), P4, P6, and P7 ( $S/D = 3$ ), and P4, P7, and P8 ( $S/D = 3.5$ ). Notably, the terminal pier P8 exhibits triple-frequency resonance at  $S/D = 3.5$ , characterized by the most complex spectral structure.

Overall, increasing the spacing ratio promotes higher dominant frequencies, especially for upstream piers, and intensifies multi-frequency resonance in midstream and downstream piers, with the terminal pier P8 displaying the most intricate resonance behavior<sup>49</sup>.

#### **Effects of pier number**

This section investigates the hydrodynamic performance of tandem bridge piers at a spacing ratio of  $S/D = 2.5$ , with an inflow velocity of 1 m/s and a corresponding Reynolds number of  $1.0 \times 10^6$ . The number of piers ( $n$ ) ranges from 2 to 10. The lift coefficient, drag coefficient, and vortex shedding frequency are analyzed to elucidate the impact of pier number on the hydrodynamic behavior and vortex shedding characteristics of the bridge piers.

#### *Lift coefficient*

Figure 16 shows the box plots of lift coefficient (CL) distribution for tandem bridge piers with different pier numbers ( $n$ ), illustrating the variation characteristics of CL under various arrangement conditions. In terms of the mean CL, certain midstream, downstream, and terminal piers exhibit more pronounced deviations from zero under specific pier numbers and positions, such as P2 ( $n = 2, 4$ ), P3 ( $n = 4, 6, 8$ ), P4 ( $n = 8$ ), P5 ( $n = 6, 10$ ), and P10 ( $n = 10$ ). This indicates that these piers are more significantly affected by upstream wake interference, resulting in a more complex hydrodynamic environment. As the number of piers ( $n$ ) increases, although the peak CL values fluctuate to some extent, the overall trend is a gradual decrease, suggesting that extreme lift effects are progressively weakened and the flow field tends to stabilize<sup>50</sup>. Overall, the midstream, downstream, and terminal piers in tandem systems experience the most significant interference in lift coefficient, while the overall hydrodynamic effects become more stable as the number of piers increases.

#### *Drag coefficient*

Figure 17 illustrates the distribution of drag coefficient (CD) for eight tandem bridge piers under different pier numbers ( $n$ ). Regarding the average CD, as  $n$  increases, the values for P1 and P2 initially decrease, then increase, and subsequently decrease again. For P3, the average CD first increases, then decreases, and finally increases once more. The average CD for P4 decreases monotonically with increasing  $n$ . Both P5 and P6 exhibit a trend of initial decrease followed by an increase in their average CD values. For P7, the average CD increases as  $n$  increases, whereas for P8, it decreases with increasing  $n$ . Among all the piers, P1 demonstrates the highest average CD, approximately 1.0, indicating that it experiences the greatest drag force. The average CD values for the remaining piers are relatively similar, at around 0.5.

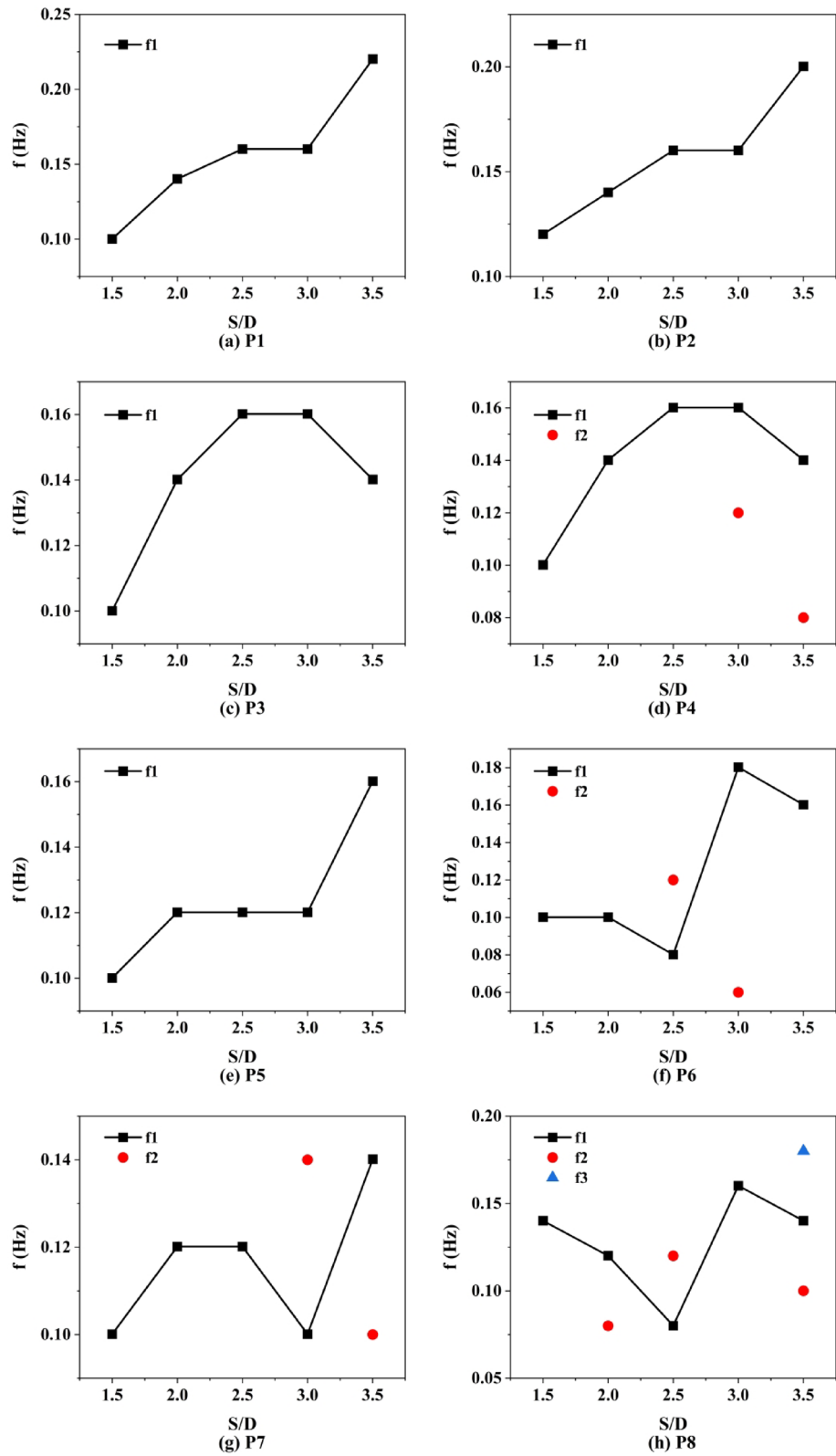
With respect to the peak CD values, P1 and P6 generally show a decreasing trend, while the peak CD values for the other piers fluctuate, exhibiting nonlinear variations. It is noteworthy that certain piers display negative CD values during specific periods, suggesting that the local flow exerts a thrust rather than a drag force. For instance, P2 exhibits negative CD values under all  $n$  conditions, and P3 demonstrates this phenomenon when  $n$  equals 6 and 8. Furthermore, except for P2, the occurrence of negative CD values for other piers diminishes as  $n$  increases.

In summary, increasing the number of piers leads to a more stable distribution of drag coefficients among the tandem bridge piers, and the force conditions for some piers are improved. Nevertheless, the leading pier continues to be subjected to the greatest drag force<sup>38</sup>.

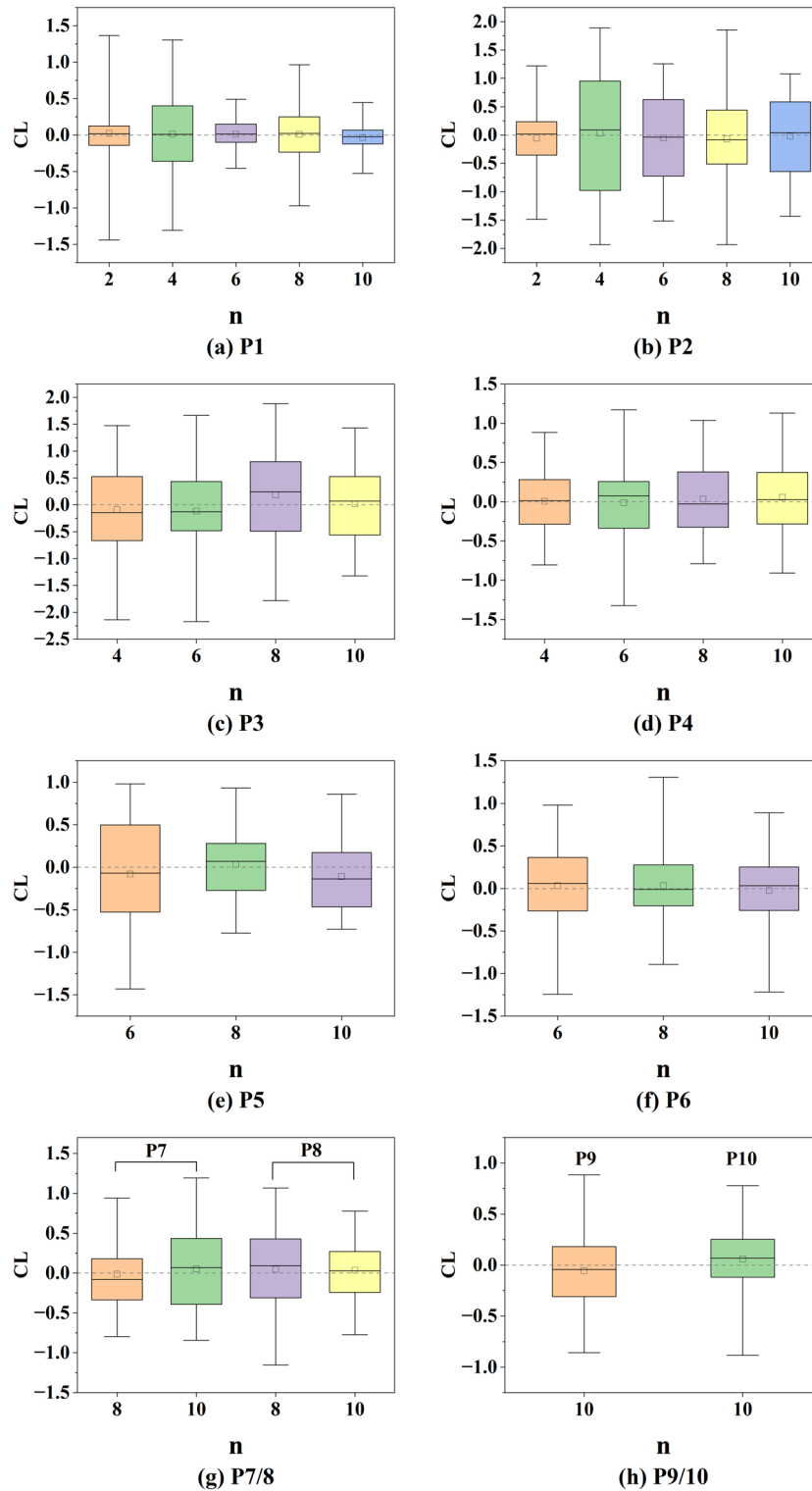
#### *Vortex shedding frequency*

Figure 18 illustrates the distribution patterns of the primary frequency ( $f_1$ ) of lift coefficients and multi-frequency resonance for each bridge pier under different numbers of piers ( $n = 2, 4, 6, 8, 10$ ), revealing the spectral response characteristics of tandem bridge piers. Regarding the primary frequency  $f_1$ , as the number of piers increases, the upstream piers (P1 and P2) maintain a relatively stable primary frequency. The midstream piers exhibit diverse trends: P3 remains stable, P4 is initially stable and then decreases, P5 gradually increases, while P6 first decreases and then increases. For the downstream piers, differentiation is evident, with the primary frequency of P7 decreasing and that of P8 increasing as  $n$  increases.

The phenomenon of multi-frequency resonance emerges earlier in the downstream piers as the number of piers increases (e.g., at  $n = 6$  for P5, and at  $n = 8$  for P6 and P8)<sup>51</sup>. When  $n$  reaches 10, multi-frequency resonance is observed not only in the downstream piers (such as P10), but also begins to expand into the midstream region



**Fig. 15.** Distribution of vortex shedding frequency for eight tandem bridge piers under varying spacing ratios ( $S/D$ ): (a) P1 to (h) P8.



**Fig. 16.** Distribution of lift coefficient (CL) for tandem bridge piers under different numbers of piers (n): (a) P1, (b) P2, (c) P3, (d) P4, (e) P5, (f) P6, (g) P7 and P8, (h) P9 and P10.

(such as P5), resulting in a more complex spectral structure. Notably, the secondary frequency  $f_2$  associated with multi-frequency resonance shows significant variation depending on pier position: for downstream piers,  $f_2$  is higher than the primary frequency  $f_1$ , while for midstream piers,  $f_2$  is lower than  $f_1$ . This can be attributed to differences in flow field disturbance intensity at various locations: downstream piers are subject to stronger cumulative disturbances, which elevate the vortex-induced frequency, causing  $f_2$  to exceed  $f_1$ ; in contrast, the

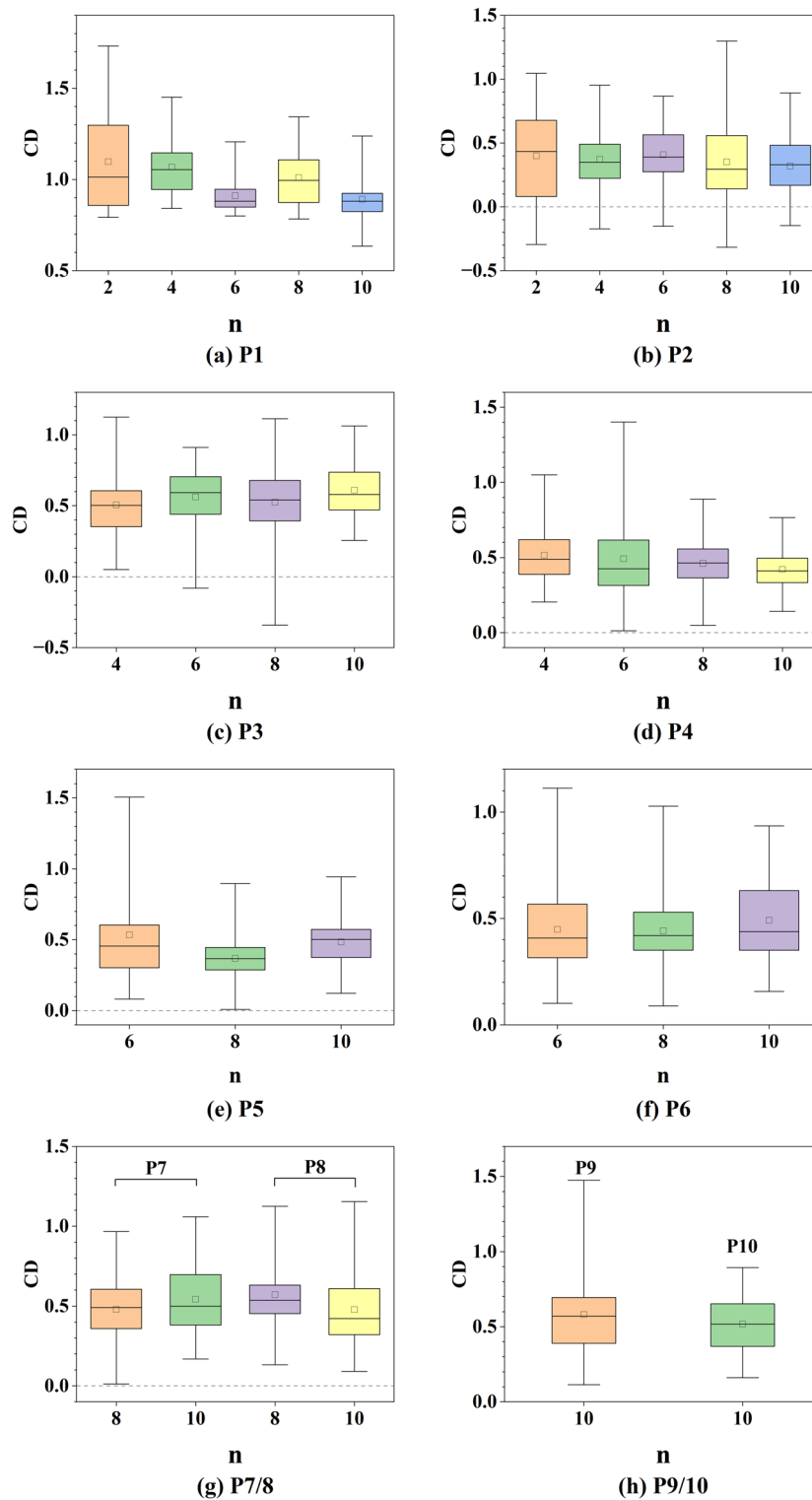


**Fig. 17.** Distribution of drag coefficient (CD) for tandem bridge piers under different numbers of piers (n): (a) P1, (b) P2, (c) P3, (d) P4, (e) P5, (f) P6, (g) P7 and P8, (h) P9 and P10.

flow field around midstream piers is more stable, and the secondary frequency is mainly influenced by local perturbations, resulting in  $f_2$  being lower than  $f_1$ .

In summary, as the number of piers increases, the primary frequency remains stable for upstream piers, while midstream and downstream piers exhibit diverse changes. Multi-frequency resonance gradually emerges and intensifies in the downstream and midstream regions, reflecting the increasing flow field interference

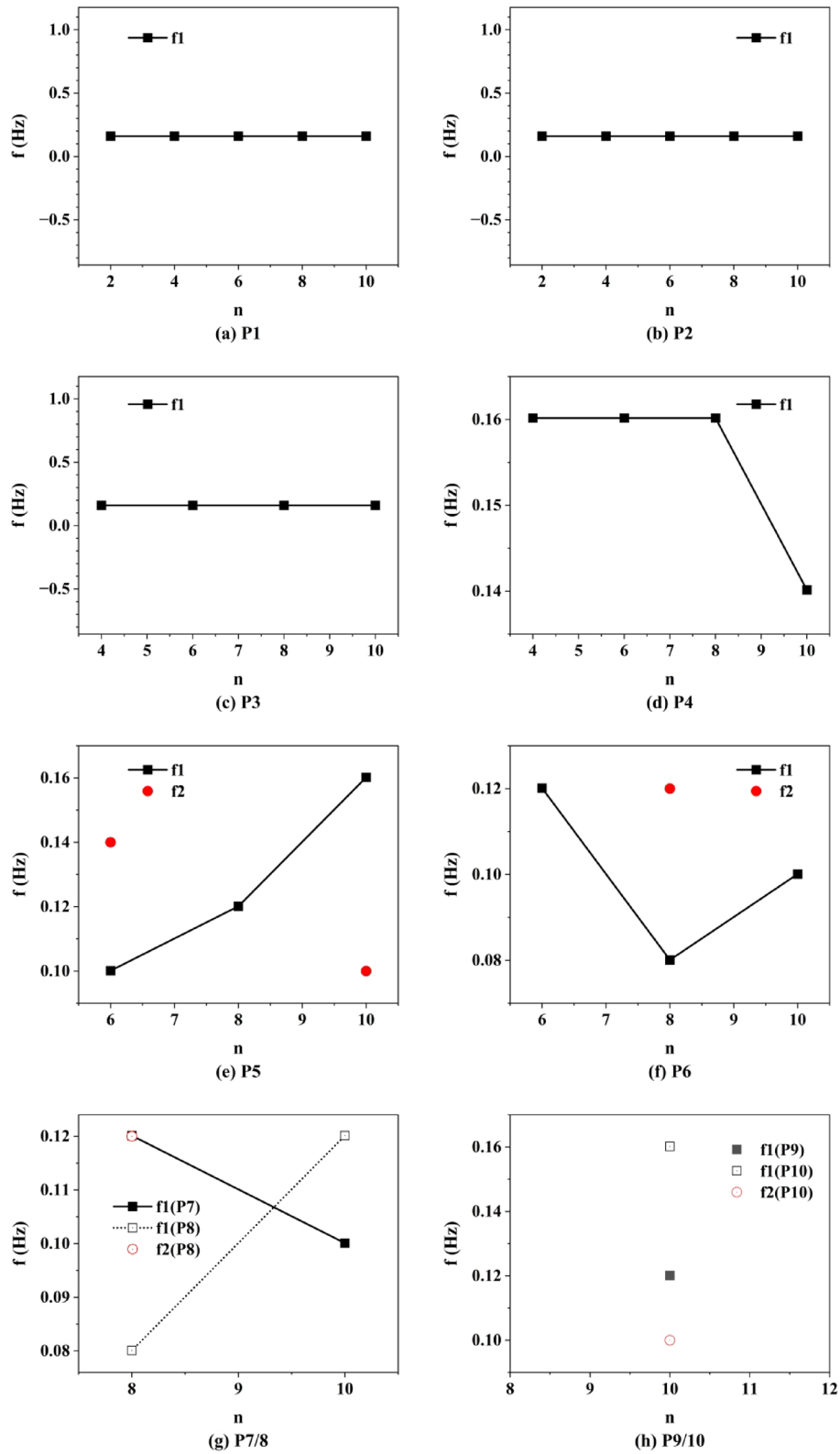


**Fig. 18.** Distribution of vortex shedding frequency for tandem bridge piers under varying numbers of piers (n): (a) P1, (b) P2, (c) P3, (d) P4, (e) P5, (f) P6, (g) P7 and P8, (h) P9 and P10.

and vortex-induced response among tandem bridge piers, as well as the pronounced differences in frequency distribution across different regions<sup>51,52</sup>.

### Limitations and future work

Despite the use of three-dimensional Large Eddy Simulation (LES) to analyze the hydrodynamic characteristics of multi-pier bridge systems, several limitations remain in this study. Firstly, LES requires significant computational resources, and the ability to accurately resolve small-scale turbulent structures is inherently restricted by grid resolution and available hardware. Secondly, the current simulation results have not been validated through laboratory experiments or higher-fidelity Direct Numerical Simulation (DNS), which may limit the robustness and generalizability of the conclusions. In future research, experimental measurements and DNS studies will be incorporated to further verify and enhance the reliability of the numerical findings. Such efforts will contribute to a more comprehensive understanding of complex flow phenomena around tandem bridge piers and improve the practical value of the research for engineering applications.

### Conclusions

This study uses Large Eddy Simulation (LES) to analyze the effects of different flow velocities ( $U$ ), spacing ratios, and pier numbers on the lift coefficient (CL), drag coefficient (CD), and vortex shedding frequency of eight equally spaced tandem bridge piers, revealing the flow field response mechanisms in multi-pier arrangements. The main conclusions are as follows:

1. Under typical conditions ( $U = 1$  m/s, spacing ratio = 2.5,  $Re = 1 \times 10^6$ ), the central region of the upstream pier exhibits the highest pressure, while the pressure points of downstream piers gradually shift laterally and the overall pressure decreases along the flow direction. The velocity distribution shows symmetric high-speed zones on both sides of upstream piers, while downstream piers exhibit alternating high and low speeds, with the wake region gradually deflecting and narrowing. Vortex structures evolve from high-intensity, small-scale upstream to expanded and diffused downstream. CL fluctuates periodically and shows spatial lag, with P3, P2, and P8 reaching the highest peaks. CD does not show a clear monotonic decrease, and some piers experience negative drag. Vortex shedding frequency is stable upstream but decreases significantly downstream, with multiple frequency resonance observed at P6 and P8.
2. Effect of flow velocity ( $U = 0.5$ – $1.5$  m/s,  $Re = 5 \times 10^5$ – $1.5 \times 10^6$ ): As  $U$  increases, the mean CL of upstream piers remains stable, while midstream piers fluctuate more at low velocity and become more stable at high velocity, with prominent peaks at P2–P4. CD trends vary by position: P1–P2 decrease, then increase, then decrease; P3–P8 increase then decrease. Negative drag can occur at different velocities. The dominant vortex shedding frequency increases with  $U$ , particularly for upstream piers, while downstream changes are less significant. Multi-frequency phenomena gradually extend from downstream to upstream and midstream as  $U$  increases.
3. Effect of spacing ratio (1.5–3.5): As spacing ratio increases, the mean CL of upstream piers remains stable, while midstream piers fluctuate markedly and peak values change nonlinearly with spacing ratio. CD of P1 peaks at spacing ratio 2.5, while P2–P8 show varied trends, with negative drag more common at smaller spacing ratios. A larger spacing ratio helps reduce flow interference. The dominant vortex shedding frequency generally increases with spacing ratio, most notably for upstream piers. Multi-frequency resonance in midstream piers becomes more pronounced with increasing spacing ratio, and the terminal pier P8 exhibits three-frequency resonance at spacing ratio 3.5.
4. Effect of pier number: As the number of piers increases, peak CL decreases overall and the flow field becomes more stable. The distribution of CD also stabilizes; P1 consistently experiences the highest average drag (about 1.0), while other piers average around 0.5. Except for P2, negative drag occurrences gradually decrease with more piers. The dominant vortex shedding frequency remains steady for upstream piers but varies for midstream piers. Multi-frequency resonance, initially seen in downstream piers, gradually extends to midstream piers as pier number increases. For downstream piers, secondary frequencies are higher than the main frequency, while for midstream piers, secondary frequencies are lower, reflecting differences in flow field interference intensity across regions.

### Data availability

All data generated or analysed during this study are included in this published article.

Received: 6 September 2025; Accepted: 26 December 2025

Published online: 31 December 2025

### References

1. Fan, G. et al. Study on scour simulation and boundary condition conversion technology for a shallow foundation bridge. *Sci. Rep.* **15**, 4581 (2025).
2. Sato, H. Model experiments on hydraulic properties around multiple piers with reproduced 3D geometries. *Sci. Rep.* **12**, 19938 (2022).
3. Pasupuleti, L. N., Timbadiya, P. V. & Patel, P. L. Flow fields around tandem and staggered piers on a mobile bed. *Int. J. Sedim. Res.* **37**, 737–753 (2022).
4. Azma, A. et al. ML and CFD simulation of flow structure around tandem bridge piers in pressurized flow. *Comput. Mater. Continua.* **75**, 1711–1733 (2023).
5. Devi, G. & Kumar, M. Experimental study of the local scour around the two piers in the tandem arrangement using ultrasonic ranging transducers. *Ocean Eng.* **266**, 112838 (2022).

6. Pasupuleti, L. N., Timbadiya, P. V. & Patel, P. L. Flow field measurements around isolated, staggered, and tandem piers on a rigid bed channel. *Int. J. Civil Eng.* **20**, 569–586 (2022).
7. Gao, P., Mou, X. & Ji, H. Simulation study on local scour characteristics of tandem bridge piers in a straight river under a changing environment. *Sustainability* **15**, 11776 (2023).
8. Wang, H., Tang, H., Xiao, J., Wang, Y. & Jiang, S. Clear-water local scouring around three piers in a tandem arrangement. *Sci. China Technological Sci.* **59**, 888–896 (2016).
9. Sharifi Ghazijahani, M. & Cierpka, C. Flow structure and dynamics behind cylinder arrays at Reynolds number  $\sim 100$ . *Phys. Fluids*. **35**, 067125 (2023).
10. Qi, H., Zheng, J. & Zhang, C. Numerical simulation of velocity field around two columns of tandem piers of the longitudinal bridge. *Fluids* **5**, 32 (2020).
11. Jiang, H. & Cheng, L. Large-eddy simulation of flow past a circular cylinder for Reynolds numbers 400 to 3900. *Phys. Fluids*. **33**, 034119 (2021).
12. Kumari, S., Tiwari, H. & Chavan, R. Advanced numerical investigation of flow field and morphological evolution around tandem piers. *Adv. Water Resour.* (2025).
13. Kumari, S., Tiwari, H. & Chavan, R. Analyzing the effectiveness of turbulence models in predicting flow around tandem piers. *Ocean Eng.* **321**, 120467 (2025).
14. Ataie-Ashtiani, B. & Aslani-Kordkandi, A. Flow field around single and tandem piers. *Flow Turbul. Combust.* **90**, 471–490 (2013).
15. Das, R., Das, S., Jaman, H. & Mazumdar, A. Impact of upstream bridge pier on the scouring around adjacent downstream bridge pier. *Arab. J. Sci. Eng.* **44**, 4359–4372 (2019).
16. Liu, Q., Tang, H., Wang, H. & Xiao, J. Critical velocities for local scour around twin piers in tandem. *J. Hydrodynamics*. **30**, 1165–1173 (2018).
17. Hashemi, M., Zomorodian, M. A. & Alishahi, M. M. Simulation of turbulent flow around tandem piers. *Iran. J. Sci. Technol. Trans. Civil Eng.* **43**, 761–768 (2019).
18. Yu, P., Liu, J., Yu, L. & Zhu, L. Numerical investigation of local scour around tandem piers using proposed self-sustaining Inlet turbulent boundary conditions. *Ocean Eng.* **274**, 113987 (2023).
19. Nandi, B. & Das, S. Developing new equations for maximum scour depth near tandem, side-by-side, and eccentric piers. *Can. J. Civ. Eng.* **52**, 1030–1044 (2025).
20. Mamoon, A. A., Zhao, M., Wu, H. & Keshavarzi, A. Experimental investigation of local scour around two submerged short square piles under tandem, side-by-side and staggered arrangements in steady current. *Ocean Eng.* **261**, 112156 (2022).
21. Zhou, J., Qiu, X., Li, J. & Liu, Y. The gap ratio effects on vortex evolution behind a circular cylinder placed near a wall. *Phys. Fluids*. **33**, 037112 (2021).
22. Guo, Y. J., Min, X. W., Cheng, X. Z. & Chen, W. L. Flow configuration improvement and vortex evolution of staggered cylinders. *J. Wind Eng. Ind. Aerodyn.* **257**, 106012 (2025).
23. Sumner, D., Price, S. & Paidoussis, M. Flow-pattern identification for two staggered circular cylinders in cross-flow. *J. Fluid Mech.* **411**, 263–303 (2000).
24. Zhou, Y., Zhang, H. & Yiu, M. The turbulent wake of two side-by-side circular cylinders. *J. Fluid Mech.* **458**, 303–332 (2002).
25. Raushan, P. K., Singh, S. K. & Debnath, K. Turbulent anisotropy and length scale variation over multiple shaped structure. *J. Offshore Mech. Arct. Eng.* **145**, 061901 (2023).
26. Golpira, A., Baki, A. B., Ghamry, H. & Katopodis, C. Influence of boulder submergence ratio on local flow field: implications for sediment and fish instream habitat. *Ecol. Eng.* **193**, 106997 (2023).
27. Grioni, M. et al. A numerical study of the flow interference between two circular cylinders in tandem by scale-adaptive simulation model. *JAFM* **13**, 169–183 (2020).
28. Ikani, N., Pu, J. H. & Soori, S. Flow pattern and turbulent kinetic energy analysis around tandem piers: insights from k- $\epsilon$  modelling and acoustic doppler velocimetry measurements. *Water* **17**, 1100 (2025).
29. Islam, S. U., Manzoor, R., Ying, Z. C. & Islam, Z. U. Numerical investigation of different aspect ratios for flow past three inline rectangular cylinders. *J. Brazilian Soc. Mech. Sci. Eng.* **40**, 410 (2018).
30. Shi, F. et al. Numerical study on hydrodynamic performance and vortex dynamics of multiple cylinders under forced vibration at low Reynolds number. *JMSE* **13**, 214 (2025).
31. Parnaudeau, P., Carlier, J., Heitz, D. & Lamballais, E. Experimental and numerical studies of the flow over a circular cylinder at Reynolds number 3900. *Phys. Fluids*. **20**, 085101 (2008).
32. Nemes, A., Zhao, J., Lo Jacono, D. & Sheridan, J. The interaction between flow-induced vibration mechanisms of a square cylinder with varying angles of attack. *J. Fluid Mech.* **710**, 102–130 (2012).
33. Ma, X. & Karniadakis, G. E. A low-dimensional model for simulating three-dimensional cylinder flow. *J. Fluid Mech.* **458**, 181–190 (2002).
34. Norberg, C. Flow around a circular cylinder: aspects of fluctuating lift. *J. Fluids Struct.* **15**, 459–469 (2001).
35. Jiang, H. & Cheng, L. Strouhal–Reynolds number relationship for flow past a circular cylinder. *J. Fluid Mech.* **832**, 170–188 (2017).
36. Sumner, D. Two circular cylinders in cross-flow: A review. *J. Fluids Struct.* **26**, 849–899 (2010).
37. Keshavarzi, A., Shrestha, C. K., Zahedani, M. R., Ball, J. & Khabbaz, H. *Experimental Study of Flow Structure Around Two in-line Bridge Piers* Vol. 171, 311–327 (Thomas Telford Ltd, 2018).
38. Tanteekin, A., Tumen Ozdil, N. F. & Akilli, H. Numerical investigation of flow around single and tandem cylindrical complex Bridge piers. *Iran. J. Sci. Technol. Trans. Mech. Eng.* 1–16 (2025).
39. Böhle, M. & Frey, T. Numerical and experimental investigations of the three-dimensional-flow structure of tandem cascades in the sidewall region. *J. Fluids Eng.* **136**, 071102 (2014).
40. Hao, P., Li, G. D., Yang, L. & Chen, G. Numerical study on flow around three circular piers in tandem arrangement at a supercritical Reynolds number. *Appl. Mech. Mater.* **170**, 1932–1937 (2012).
41. Alam, M. M. Lift forces induced by phase lag between the vortex sheddings from two tandem bluff bodies. *J. Fluids Struct.* **65**, 217–237 (2016).
42. Sikdar, P., Dash, S. M. & Lua, K. B. Vortex structure manipulation and drag reduction of tandem circular cylinders using a pitching splitter plate. *Phys. Fluids*. **36**, (2024).
43. Li, J., Wu, B., Ma, C., Cui, B. & Li, S. Flow patterns and vortex related characteristics of tandem rectangular structures with recessed corners. *Phys. Fluids* **37**, (2025).
44. Yang, X., Qian, J. & Weng, S. Determination of equivalent roughness of bridge piers' flow resistance. *J. Hydrol. Eng.* **24**, 04019024 (2019).
45. Kouchakzad, M., Sohankar, A. & Rastan, M. Onset of vortex shedding and hysteresis in flow over tandem sharp-edged cylinders of diverse cross sections. *Phys. Fluids*. **36**, (2024).
46. Zeng, C., Zhang, Y., Qiu, F., Zhou, J. & Wang, L. Large eddy simulation of flow around two tandem circular cylinders at a Reynolds number of 3900. *Phys. Fluids*. **37**, (2025).
47. He, Z., Yuan, H., Wang, G. & Tu, J. Effect of spacing ratios on coupling mechanism of three tandem cylinders in planar shear flow. *Ocean Eng.* **291**, 116312 (2024).
48. Lankadasu, A. & Vengadesan, S. Interference effect of two equal-sized square cylinders in tandem arrangement: with planar shear flow. *Int. J. Numer. Methods Fluids*. **57**, 1005–1021 (2008).

49. Hammad, O. S. & Mohany, A. Vortex shedding characteristics and hydrodynamic forces of stationary and elastically mounted side-by-side cylinders fitted with small diameter control rods. *J. Fluids Struct.* **120**, 103908 (2023).
50. Tan, Z., Chen, W., Chen, B. & Wang, Y. Quantitative analysis of the effect of pier turbulence on ship yaw moment. Vol. 2002, 012067 (IOP Publishing, 2021).
51. Zhu, H., Zhong, J. & Zhou, T. Wake structure characteristics of three tandem circular cylinders at a low Reynolds number of 160. *Phys. Fluids.* **33**, (2021).
52. Zhu, H., Xu, B., Alam, M. M., Gao, Y. & Zhou, T. Vortex-induced vibration and hydrodynamic characteristics of a round-ended cylinder. *Ocean Eng.* **284**, 115284 (2023).

## Acknowledgements

The National Natural Science Foundation of China (Grant number 51978674), Guangzhou Municipal Construction Group (Grant number. [2023]-KJ045)

## Author contributions

W.L. (Weigun Liang) performed the software development, validation, formal analysis, and investigation, curated and visualized the data, and drafted the original manuscript. X.C. (Xiaobin Chen) contributed resources, methodology, and validation. L.T. (Lubo Tang) conceived the study (conceptualization) and provided supervision. J.Z. (Jiasheng Zhang) contributed to methodology and writing – review & editing. J.C. (Jun Cheng) contributed to data curation. All authors reviewed and approved the final manuscript.

## Funding

The National Natural Science Foundation of China (Grant Numbers 51978674); Guangzhou Municipal Construction Group (Grant Number [2023]-KJ045).

## Declarations

### Competing interests

The authors declare no competing interests.

## Additional information

**Correspondence** and requests for materials should be addressed to X.C.

**Reprints and permissions information** is available at [www.nature.com/reprints](http://www.nature.com/reprints).

**Publisher's note** Springer Nature remains neutral with regard to jurisdictional claims in published maps and institutional affiliations.

**Open Access** This article is licensed under a Creative Commons Attribution-NonCommercial-NoDerivatives 4.0 International License, which permits any non-commercial use, sharing, distribution and reproduction in any medium or format, as long as you give appropriate credit to the original author(s) and the source, provide a link to the Creative Commons licence, and indicate if you modified the licensed material. You do not have permission under this licence to share adapted material derived from this article or parts of it. The images or other third party material in this article are included in the article's Creative Commons licence, unless indicated otherwise in a credit line to the material. If material is not included in the article's Creative Commons licence and your intended use is not permitted by statutory regulation or exceeds the permitted use, you will need to obtain permission directly from the copyright holder. To view a copy of this licence, visit <http://creativecommons.org/licenses/by-nc-nd/4.0/>.

© The Author(s) 2026